Induced polarization of volcanic rocks – 6: relationships with other petrophysical properties

K Zhang, N Chibati, André Revil, J Richard, M Gresse, Y Xue, Y Géraud

Geophysical Journal International

Geophys. J. Int. (2023) **234,** 2376–2394
Advance Access publication 2023 June 19
GJI Heat Flow and Volcanology

https://doi.org/10.1093/gji/ggad246

Induced polarization of volcanic rocks – 6: relationships with other petrophysical properties

K. Zhang,[1,2] N. Chibati,[3] A. Revil,[2] J. Richard,[2] M. Gresse,[4] Y. Xue[5] and Y. Géraud[3]

[1]*Research Center of Geotechnical and Structural Engineering, Shandong University, Shandong Province, Jinan* 250061*, China*
[2]*Université Grenoble Alpes, Université Savoie Mont-Blanc, CNRS, UMR CNRS* 5204*, EDYTEM, Le Bourget du Lac, France. E-mail: andre.revil@univ-smb.fr*
[3] *Université de Lorraine, UMR* 7359 *GeoRessources, Ecole Nationale Supérieure de Géologie,* 2 *Rue du Doyen Marcel Roubault, Vandoeuvre-lès-Nancy* 54500*, France*
[4]*Research Institute of Earthquake and Volcano Geology, Geological Survey of Japan, AIST, Tsukuba, Japan*
[5]*School of Engineering and Technology, China University of Geophysics, Beijing* 100083*, China*

Accepted 2023 June 16. Received 2023 June 15; in original form 2023 March 2

SUMMARY

The petrophysical properties of 41 volcanic samples from La Soufrière volcanoe (Guadeloupe Island, Eastern Caribbean, France) are investigated. We first measure the complex conductivity spectra of these rock samples at 4 salinities (NaCl) at laboratory conditions (∼20 °C). For each rock sample, we determine the (intrinsic) formation factor, the surface conductivity and the Cole–Cole normalized chargeability. We also measure the compressional wave velocity (dry and saturated), the shear wave velocity in saturated conditions, the (dry and saturated) thermal conductivity, the dry specific heat capacity and the permeability of the rock samples as well as their cation exchange capacity (CEC) and connected porosity. The formation factor versus porosity obeys Archie's law with a cementation exponent of 2.16 ± 0.10. The surface conductivity and the normalized chargeability are proportional to each other and to the CEC divided by the tortuosity of the material (product of the formation factor by the connected porosity) as predicted by the dynamic Stern layer model. Permeability can be predicted from the normalized chargeability and the formation factor inside one order of magnitude. The thermal conductivity and the seismic properties can be evaluated from the connected porosity of the core samples formation factors. A non-linear relationship is established between the shear wave velocity and the compressional wave velocity for the present data set and other data from the literature. Finally, we show on a specific example, how to convert an induced polarization survey on a stratovolcano into a seismic velocity model (*P*- and *S*-waves velocity distributions). We perform a specific application to Papandayan Volcano, a stratovolcano located in Java Island (Indonesia). This work paves the way to the joint inversion problem of seismic and induced polarization surveys for volcanic unrest monitoring.

Key words: Electrical properties; Permeability and porosity; Seismic velocities; Induced polarization; Volcanoes.

1 INTRODUCTION

Volcanic activity is characterized by changes in temperature, fluid content, fluid pressure; petrology, deformation and stress (including fault reactivation) and topography in responses to magmatic forcing. The spatial and temporal distribution of these variations are observed by gravity, electrical and seismic signals, as well as surface manifestations (emissions of magna, vapour and water) inducing thermal changes (e.g. Bonafede 1991; Rinaldi *et al.* 2011; Fournier & Chardot 2012; Minami *et al.* 2018; Hill *et al.* 2020). The modelling of these observations for volcanic unrest necessitates the non-intrusive characterization of magmatic and hydrothermal effects through the use of geophysical methods and numerical modelling approaches (Todesco & Berrino 2005; Jasim *et al.* 2015; Petrillo *et al.* 2019; Carbonari *et al.* 2019; Heap *et al.* 2020; Stissi *et al.* 2021; Gola *et al.* 2021 Zhan *et al.* 2022). Such goal requires a consistent modelling of the petrophysical properties of interest (e.g. Gottsmann *et al.* 2008, 2020; Heap *et al.* 2022a,b; Iwamori *et al.* 2021 Watanabe *et al.* 2022) and to connect these properties to those measured or imaged through geophysical investigations techniques (e.g. Revil *et al.* 2003; Finizola *et al.* 2006; Jardani & Revil 2009; Karaoulis *et al.* 2014; Navelot 2018).

In the two first papers of this series (Revil *et al.* 2017a, b), we have developed a petrophysical model for the induced polarization of volcanic rocks. Then the model was applied to image the clay cap

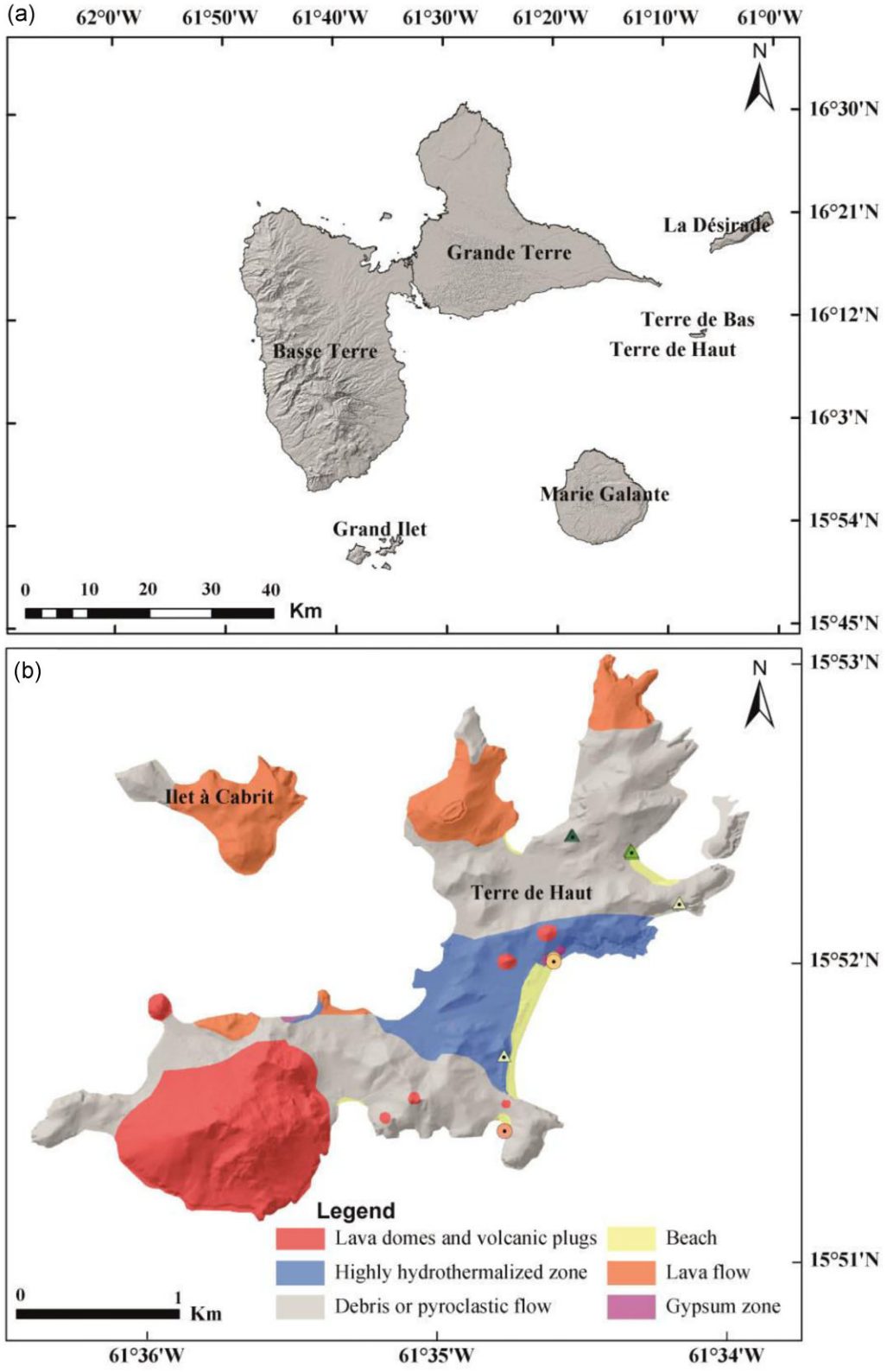

Figure 1. Maps. (a) Guadeloupe archipelago (Digital Elevation Map, DEM, from IGN, Institut Géographique National). Inset map showing the geodynamic setting of the Lesser Antilles arc (after Favier *et al.* 2021; Feuillet *et al.* 2001; heat flow measurements from Manga *et al.* 2012). (b) Geological maps of Terre de Haut (from Varati *et al*. 2016).

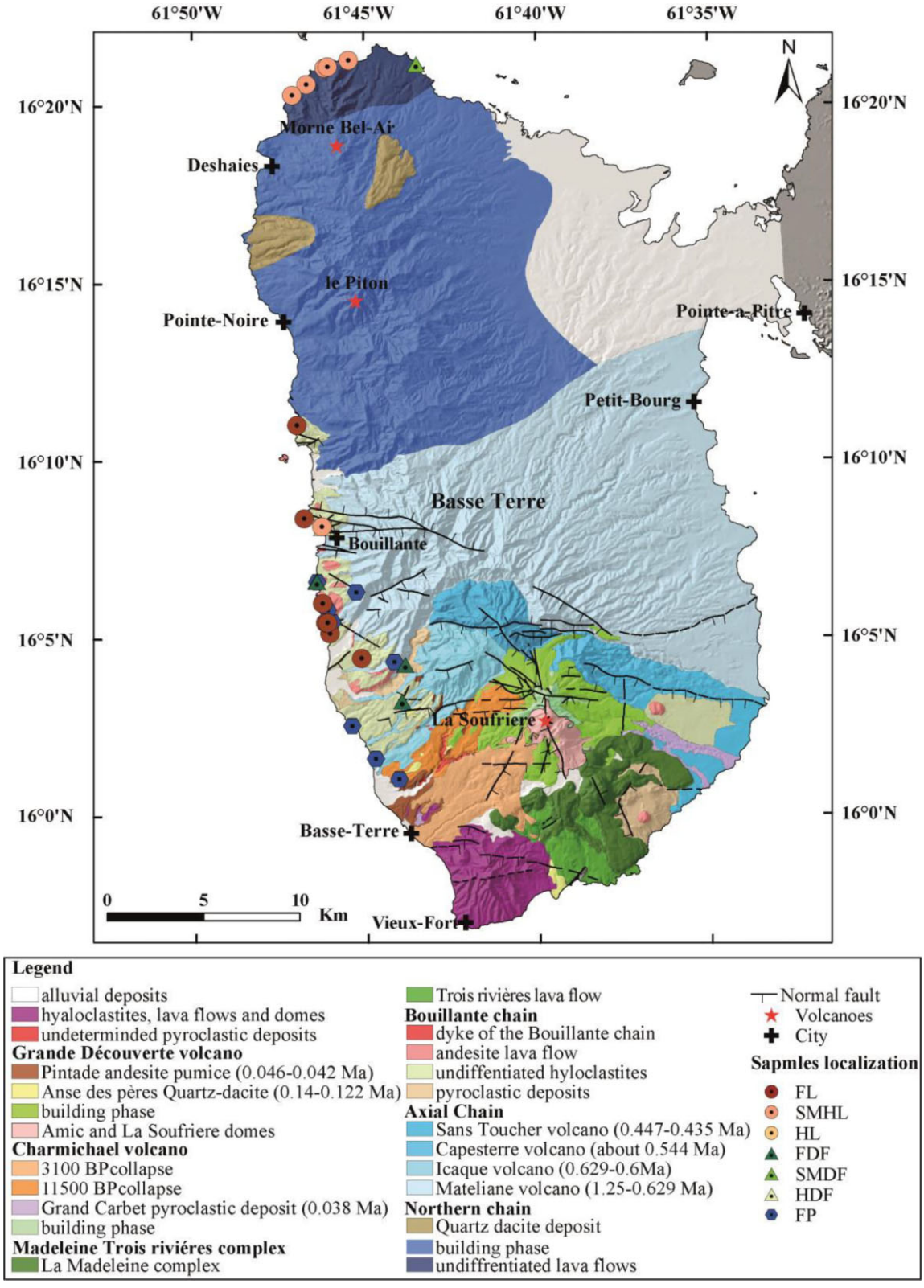

Figure 2. Localization of the core samples and geological maps of Basse Terre (after Mathieu 2010; Navelot 2018).

of the hydrothermal system in volcanic areas (Revil *et al.* 2019) and to image shield volcanoes in terms of alteration and temperature distributions (Revil *et al.* 2021). One of the results obtained in these papers is that surface conductivity associated with conduction in the electrical double layer coating the surface of the grains cannot be neglected (see also Komori *et al.* 2013; Soueid Ahmed *et al*. 2018) despite the fact it is still often neglected even in recent papers (e.g. Matsunaga & Kanda 2022). A second observation is that surface

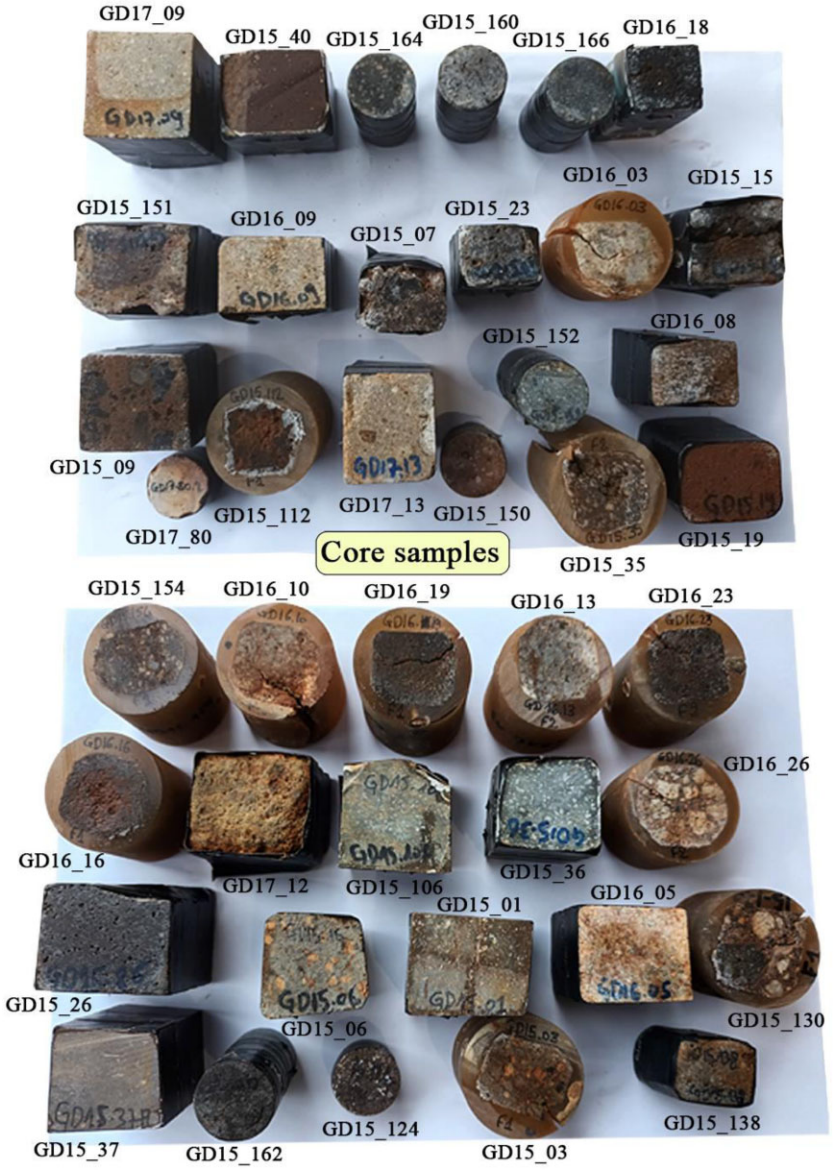

Figure 3. Picture of the core samples used in this study (41 core samples shown here). They include fresh lava, fresh and altered debris flow and altered lava.

conductivity, quadrature conductivity, and normalized chargeability can be related to each other.

Our goal in this paper is to develop robust empirical relationships between petrophysical properties of interest including electrical conductivity, normalized chargeability, the seismic compressional and shear wave velocities, the thermal conductivity, the specific heat capacity and the permeability together with the cation exchange capacity (CEC) and the connected porosity of the rock samples. In order to reach this goal, we further expanded a database of petrophysical properties (see https://petrophysics.otelo.univ-lorraine.fr) by the acquisition of a novel data set using a set of 41 volcanic rock samples from the stratovolcano of La Soufrière (Guadeloupe Island, Eastern Caribbean, France, Figs 1 and 2). Whenever possible, we will compare this data set to other available data from the literature, especially those associated with andesites from stratovolcanoes.

In the last part of this study, we investigate the relationship between induced polarization and *P*- and *S*-wave velocities at Papandayan stratovolcano (Java Island) in Indonesia as well as with connected porosity and CEC. We show that we can reconstruct seismic tomograms from an induced polarization survey with an application to Papandayan stratovolcano. Such a work could be used for the development of future joint inversion schemes (for instance petrophysics-based) for seismic and electrical/electromagnetic data to monitor the volcanic unrest of active volcanoes.

2 PETROPHYSICAL STUDY

In this section, we present the work done in acquiring a new data set of petrophysical data on the same set of core samples. In the next section, these data will be analysed in terms of simple petrophysical relationships.

2.1. Core samples

We selected 41 core samples from La Soufrière volcano (Figs 1 and 2). The samples are lavas and debris flow deposits from fresh

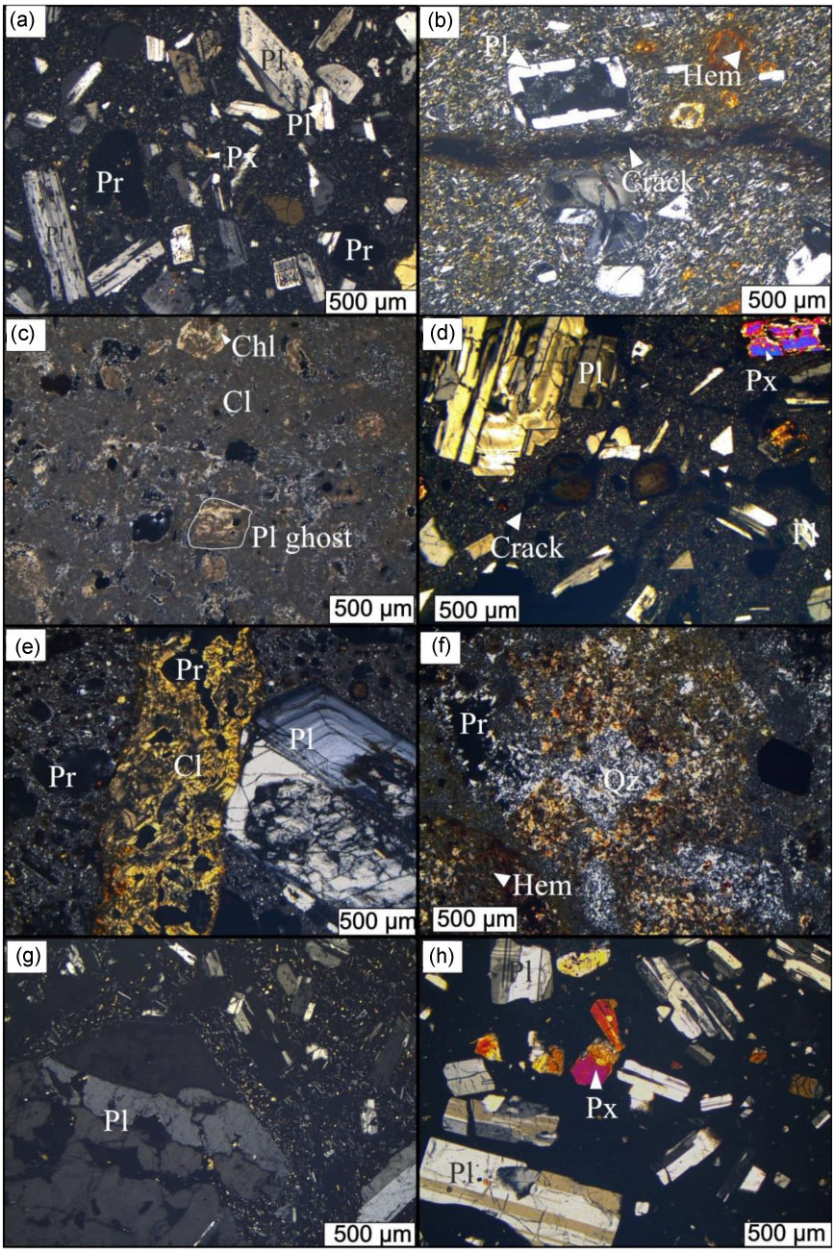

Figure 4. Typical thin sections. (a) Fresh lava (FL). (b) Slight to mean altered lave (SML). (c) hydrothermalized lava (HL) (d) Fresh debris flow (FDF). (e) Slight to mean altered debris flow. (f) Hydrothermalized debris flow. (g) and (h) Fresh pyroclastic deposit. Abreviations: Cl, clay; chl, chlorite; Hem, hematite; Pl, plagioclase; Px, pyroxene; Pr, porosity and Qz, quartz.

states to samples exhibiting different degrees of alteration (Figs 3 and 4).

Fresh lava core samples (labelled FL below) with various degree of vesicularity have phenocrysts of plagioclase, orthopyroxene, clinopyroxene and magnetite from 500 µm to 2 mm in size, these minerals are also present as microcrysts, and the glass phase amount is low. The slightly to moderate altered lava facies corresponds to vesicular lava, phenocrysts similar to the fresh facies are slightly altered, cracks and vesicles partly filled by secondary minerals Ti- Fe-Mn-oxydes, baryte, calcite, pyrite, chlorite and muscovite (Favier *et al.* 2021). Fresh debris flows (FSF) are formed by centimetric to decametric clasts englobed in matrix of different compositions. In clasts the composition and the texture are similar to those of fresh lava material. The matrix is composed by the same primary mineral assemblage with clay and oxides, their grains size could be largely lower (Navelot *et al.* 2018). For moderately altered facies, plagioclases are generally not affected, and pyroxenes are largely dissolved and replaced by clayey minerals, actinolite, pyrite and quartz. For highly altered facies initial phenocrysts, mesostase, and glass matrix are recrystallized to clay, iron oxide, pyrite, calcite and quartz mineral (see Navelot 2018; Heap *et al.* 2022a,b). Among these minerals, pyrite can have a strong polarization. It seems however that the total amount of pyrite is small (<3 per cent weight) enough to be sure that the polarization of pyrite is not dominating the overall polarization response.

The CEC measurements were performed with the cobalt hexamine method using 2 g of crushed rocks and a calibrated spectrophotometer working at 472 nm (see the procedure in Aran *et al.*

Table 1. Properties of the core samples. The pH is the equilibrium pH of the solution for the cation exchange capacity measurements. Note that the pH of the solution in equilibrium with the core samples varies from neutral to strongly acidic, an expected results for stratovolcanoes. The quantity S_{sp} denotes the specific surface area of the core samples. A qualitative description of the rock samples is: FL: Fresh lava, SMDF: Poorly altered debris flow, HDF: strongly altered debris flow, FDF: Fresh debris flow, FP: Fresh pyroclastic deposits, and SML: Poorly altered lava. The CEC is expressed in meq (100 g)$^{-1}$ [1 meq (100 g)$^{-1}$ = 963.20 C kg^{-1} in SI units]. The permeability k is the nitrogen-gas permeability. The surface conductivity is determined from the in-phase conductivity measured at 1 Hertz. Some samples disintegrated in the course of the experiments.

Full name	Type	Porosity ϕ (–)	CEC (meq (100 g)$^{-1}$)	pH (–)	ρ_g (kg m^{-3})	k (m^2)	F (–)	σ_S (S m^{-1})
GD15_01	SML	0.0295	18.7	-	2540	3.80E-19	1499	0.0229
GD15_03	SMDF	0.2906	18.5	5.05	2610	1.54E-15	20.1	0.0294
GD15_06	SMDF	0.2501	18.3	5.80	2540	2.60E-14	50.3	0.0270
GD15_07	FDF	0.3418	21.2	6.47	2490	-	14.9	0.0250
GD15_09	FDF	0.3412	26.3	6.78	2570	1.40E-13	14.0	0.0430
GD15_106	FL	0.0354	3.7	7.71	2690	1.10E-19	612	0.0074
GD15_112	FP	0.5104	18.6	6.15	2640	2.84E-12	12.2	0.0476
GD15_124	FDF	0.4350	17.7	6.31	2790	8.86E-14	108	0.0062
GD15_130	FDF	0.3708	9.4	5.54	2640	1.30E-13	23.7	0.0107
GD15_138	SMDF	-	19.4	-	2650	1.40E-15	31.9	0.0274
GD15_15	FP	0.2162	4.2	7.95	2720	1.10E-14	65.8	0.0022
GD15_150	SML	0.2596	4.95	5.50	2630	4.40E-13	23.3	0.0170
GD15_151	HDF	0.1189	6.7	8.96	2620	3.20E-16	112.6	0.0063
GD15_152	FL	0.0239	13.5	6.27	2750	3.70E-19	4735	0.0019
GD15_154	FDF	0.4476	25.2	7.30*	2460	4.10E-14	30.2	0.0210
GD15_160	FL	0.1268	2.88	8.57	2740	2.10E-16	90.0	0.0039
GD15_162	FL	0.1020	6.86	7.85	2810	1.70E-16	495	0.0017
GD15_164	FL	0.0301	7.78	6.99	2610	4.10E-17	1372	0.0042
GD15_166	FL	0.0322	7.80	8.49	2830	6.90E-18	714	0.0030
GD15_19	FP	0.4196	18.9	6.69	2610	2.50E-13	10.6	0.0284
GD15_23	FL	0.1239	9.1	-	2790	8.30E-13	98	0.0028
GD15_26	FL	0.1137	4.6	8.00	2730	1.00E-15	105	0.0030
GD15_35	SML	0.2666	25.0	5.64	2570	-	13.6	0.0662
GD15_36	SML	0.0250	5.9	7.63	2660	1.00E-19	876	0.0083
GD15_37	SML	0.0216	19.7	-	2620	2.10E-17	5453	0.0210
GD15_40	SML	0.1254	5.8	7.44	2740	1.20E-15	41.8	0.0028
GD16_03	HL	0.2605	24.0	-	2740	3.60E-14	34.3	0.0183
GD16_05	HL	0.2288	14.4	-	2800	1.20E-17	58.5	0.0174
GD16_08	FDF	0.1747	7.5	7.28	2770	1.10E-15	26.3	0.0063
GD16_09	FDF	0.2295	22.0	6.86	2650	1.30E-15	25.7	0.0447
GD16_10	HDF	-	34.9	-	2650	5.06E-16	18.7	0.0480
GD16_13	FDF	0.3115	15.3	5.72	2710	4.47E-15	65.8	0.0208
GD16_16	FP	0.4477	13.9	5.60	2600	1.44E-12	16.1	0.0357
GD16_18	FP	0.3815	14.0	6.05	2680	3.00E-12	24.2	0.0022
GD16_19	FP	0.3633	21.6	7.22	2680	2.99E-13	21.0	0.0093
GD16_23	FP	0.3682	15.2	5.94	2210	2.80E-13	28.1	0.0185
GD16_26	FP	0.4389	19.2	5.74	2480	1.70E-13	46.1	0.0200
GD17_09	SML	0.1797	3.1	6.71	2560	-	48.3	0.0293
GD17_12	SMDF	0.2572	17.5	7.84	2650	-	8.6	0.0602
GD17_13	SMDF	0.2622	21.2	5.74	2660	-	30.4	0.0662
GD17_80	HDF	0.0295	29.6	4.28	-	-	10.9	0.0209

2008, see also Revil *et al.* 2017a, b, for some specific examples using volcanic rocks). The CEC is an important parameter providing a proxy for the degree of alteration of these rocks especially regarding the amount of clay minerals, illite, kaolinite, chlorite and zeolite (Revil *et al*. 2002). Since smectite is characterized by the highest high CEC ∼80 meq (100 g)$^{-1}$ (Chiou & Rutherford 1997), its presence quickly dominates the CEC of the whole rock. The CEC values of our core samples are reported in Table 1 and ranges from 3 to 35 meq (100 g)$^{-1}$ for the most altered specimens. The pH of the solutions was not buffered and the values are also reported in Table 1.

2.2. Induced polarization measurements

Induced polarization is a geophysical method related to the polarization of the electrical double layer coating non-metallic grains (Vaudelet *et al.* 2011). Frequency-domain induced polarization measurements were performed over the frequency range 10 mHz–45 kHz using the ZELSIP04-V02 impedance meter (Zimmermann *et al.* 2008, 2019 and Fig. 5). We used the core holder described in Revil *et al.* (2022) and shown in Figs 3 and 4. We measured the complex-valued impedance (amplitude and phase). The impedance is then converted to a complex conductivity with a geometrical

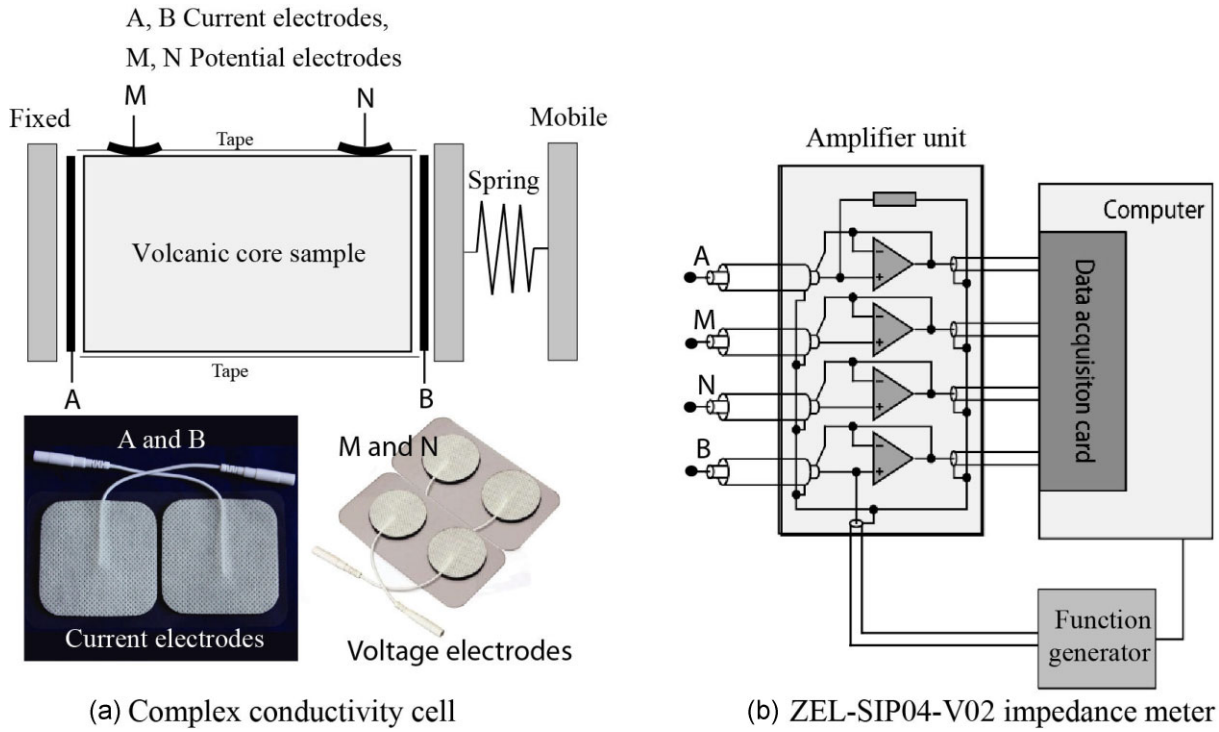

Figure 5. Spectral induced polarization measurements for the volcanic rock samples used in this study. (a) Sketch of the experimental setup for the core samples. The electrodes are self-adhesive carbon/Ag/AgCl electrodes with hydrogel used to get a low contact resistance between the core samples and the impedance meter. (b) Sketch of the ZELSIP04-V02 impedance meter used to measure the complex conductivity spectra. It operates in the frequency range 1 mHz–45 kHz (see Zimmerman *et al.* 2008, 2019).

factor depending on the position of the electrodes and boundary conditions for the electrical potential around the core surface external boundary (see Jougnot *et al.* 2010, for details).

For the core samples from La Soufrière volcano, four saline solutions were used corresponding to the following pore water conductivities σ_w (NaCl, 25 °C) = 0.08, 0.49, 4.89 and 9.45 S m^{-1}. The samples were first washed in demineralized water to remove the salt. Then they were dried and saturated under vacuum at few Pascals with the brine at the lowest salinity (0.08 S m^{-1}), which was first degassed. The spectra were done after two weeks to be sure that full saturation is obtained. Then the samples are immersed in a bath with the second salinity (0.49 S m^{-1}). The conductivity of some samples is monitored until a plateau is reached (∼4 weeks). Then, again the spectra are measured. The same procedure is repeated until the highest salinity is reached.

Fig. 6 shows complex conductivity spectra for one core sample at different salinities (Figs 6a and b). Figs 6(c) and (d) show the influence of the CEC on the complex conductivity spectra of three core samples characterized by distinct CEC values. Both the magnitude of the in-phase and quadrature conductivities increases with both the salinity and the CEC. This is consistent with previous works using volcanic rock samples (e.g. Revil *et al.* 2022, and references therein). The results are also consistent with an induced polarization model of the electrical double layer combined with speciation models for silicates and called the dynamic Stern layer model (see Revil *et al.* 2022, and references therein).

In Fig. 7, we show for some selected rock samples the influence of the pore water conductivity σ_w (S m^{-1}) on the in-phase conductivity of the rock samples σ' (S m^{-1}, measured at 1 Hz). The in-phase conductivity has two contributions, one associated with the pore netweork saturated with the pore water and the second associated with the conduction in the electrical double layer coating the surface of the grains (Waxman & Smits 1968). The relationship between the two parameters is given by (e.g. Waxman & Smits 1968; Revil *et al.* 2017a, b)

$$\sigma' = \frac{\sigma_w}{F} + \sigma_S. \tag{1}$$

To determine the values of the (intrinsic) formation factor F (dimensionless) and the value of the surface conductivity σ_S (S m^{-1}), we invert the data in the log–log domain to be sure the low salinity data are correctly accounted for in the determination of the surface conductivity. Therefore, we use the following non-linear relationship to perform the fit (see Fig. 7a),

$$Y = \log\left(\frac{10^X}{F} + \sigma_S\right), \tag{2}$$

where $Y \equiv \log\sigma'$ and $X \equiv \log\sigma_w$. Eq. (2) is used in order to get a better estimate of the surface conductivity with respect to the determination of this parameter based on eq. (2). The values of both the (intrinsic) formation factor and surface conductivity are reported in Table 1 for each core sample. As shown in Fig. 7(b) (for five samples with the same formation factors but distinct CEC and porosity values), the normalized conductivity ratio (rock conductivity divided by the pore water conductivity) is dependent on the ratio between the CEC, the porosity and the pore water conductivity.

2.3. Other measurements

The other properties of interest are the porosity, the grain density, the permeability, the thermal conductivity, the specific heat capacity and the shear and compressional wave velocities in saturated

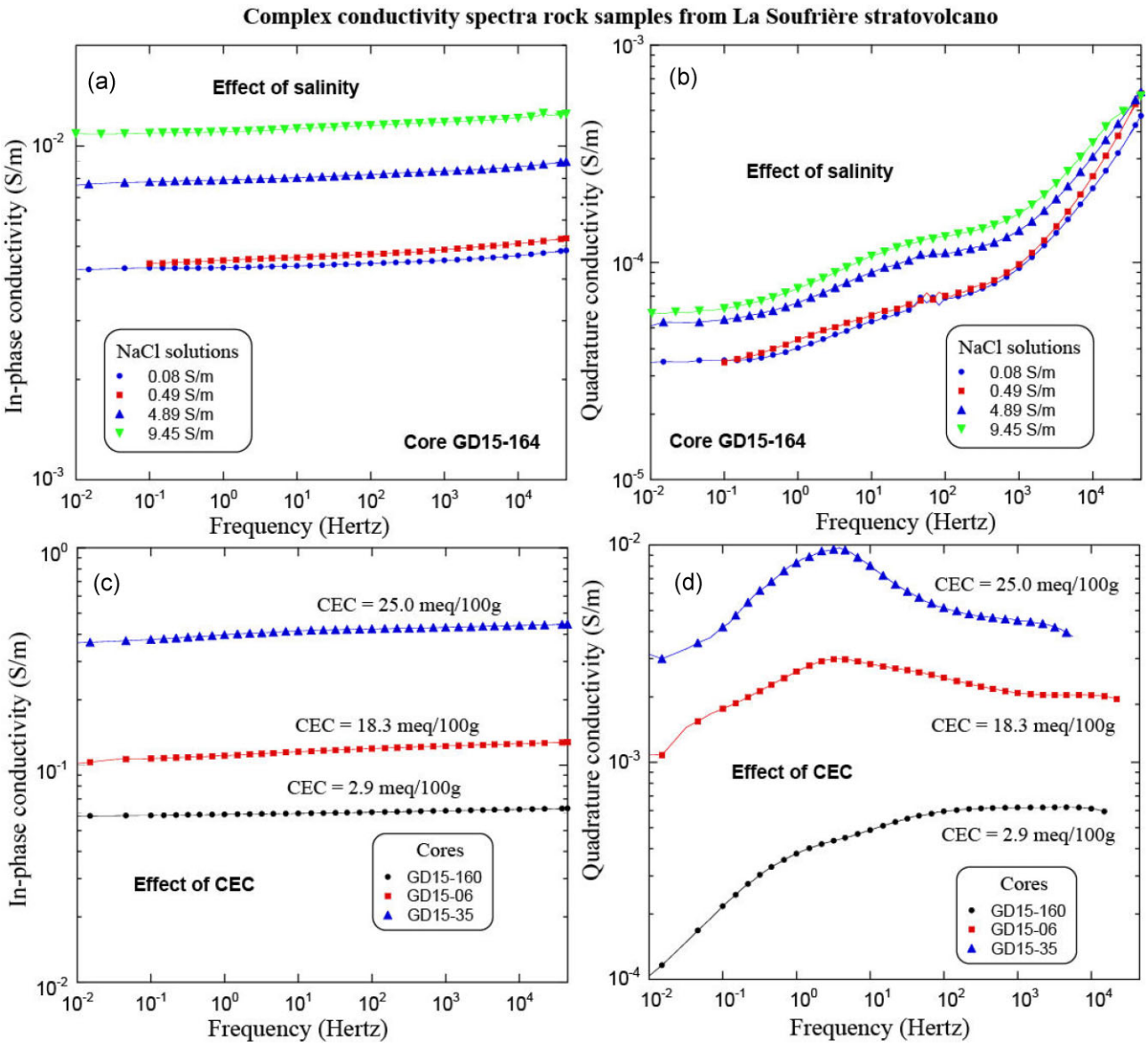

Figure 6. Influence of the salinity and cation exchange capacity (CEC) on the complex conductivity spectra of the volcanic rocks from la Soufrière volcano (Guadeloupe Island). (a) Influence of salinity on the in-phase conductivity [the CEC of GD15-164 is 7.78 meq$(100\ g)^{-1}$]. (b) Influence of salinity on the quadrature conductivity for the same core sample. (c) Influence of the CEC on the in-phase conductivity. (d) Influence of the CEC on the quadrature conductivity. The lines are guides for the eyes.

and unsaturated conditions. The grain density was obtained with a helium pycnometer (AccuPyc II 1340 of micromeritic®, see details in Anovitz & Cole 2015). The grain density was measured five times on the dry core samples and then averaged. It ranges from 2500 to 2800 kg m^{-3} (the low values may indicate the presence of non-connected porosity in the core samples). The relatively low values of the grain densities imply that the fractions of pyrite or magnetite are small.

The (connected) porosity of the core samples (reported in Table 1) was determined using the classical triple weighting method (RILEM norm, see Anovitz & Cole 2015). For this purpose, the core samples were first dried in the oven at 60 °C until they reach stable (dry) weights. Porosity values range 2–50 per cent, lower values are measured for fresh lava with low vesicular content. The high porosity values are obtained for fresh debris. The intermediate values concern the altered core samples.

The gas permeability was measured on the core samples under a confining pressure of 20 bars (∼2 MPa) using a nitrogen permeameter following the method prescribed by Rosener (2007). During the experiment, compressed nitrogen was injected into the sample at four pre-defined pressures from 1 to 18 bars (∼0.1–1.8 MPa). Once steady-state flow is reached, the permeability is calculated using Darcy's law at each pressure level. The values are reported in Table 1. Permeability ranges from 10^{-12} m^2 (∼1 Darcy) to 10^{-19} m^2 (∼0.1 μD). The data shown in Table 1 are corrected for the Klinkenberg effect.

A thermal conductivity scanner (TCS) from Lippmann & Rauen GbR was used to measure the thermal conductivity and the thermal

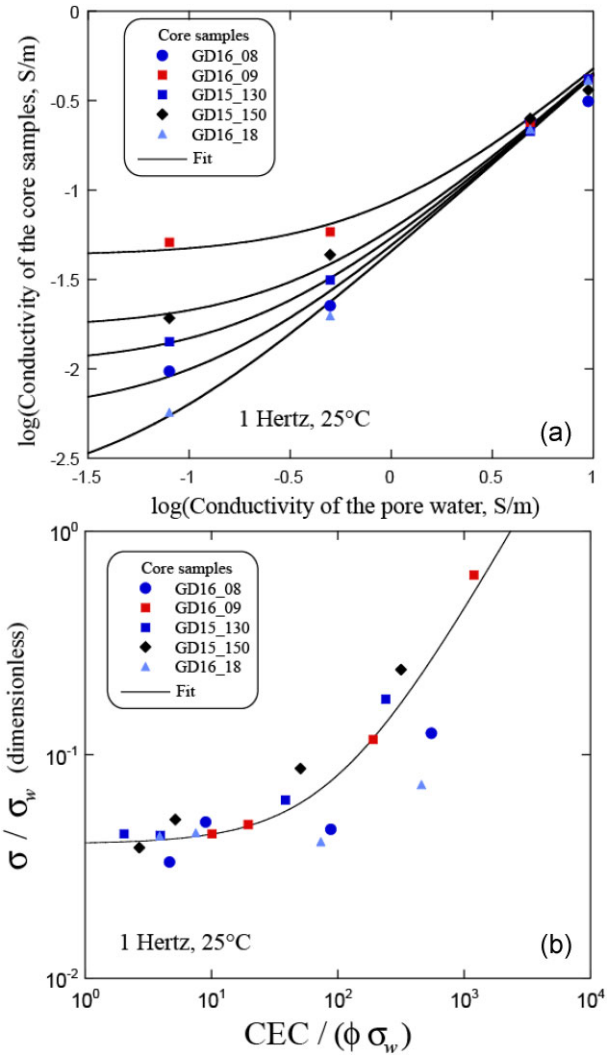

Figure 7. Influence of the salinity and CEC on the in-phase conductivity data. (a) In-phase electrical conductivity of the rock samples versus the conductivity of the pore water (NaCl solutions, 25 °C, data at 1 Hz) for five samples with the same formation factor and different surface conductivities. The best fit of the non-linear relationship between the two parameters in a log-log scale (adapted from eq. 1) is used to estimate for each core sample the (intrinsic) formation factor F and the surface conductivity σ_s. (b) Normalized conductivity ratio versus the cation exchange capacity [CEC in meq (100 g)$^{-1}$] normalized by the product of the porosity by the pore water conductivity ($r^2 = 0.81$, slope 0.0103). All the samples have the same formation factors in this example.

diffusivity of the rock samples under dry and saturated conditions. The measurement procedure was detailed in Popov *et al.* (1999, 2016); Boulanouar *et al.* (2013) and Haffen *et al.* (2017). The TCS method is a contactless optical scanning method developed by Popov *et al.* (1999). The Specific heat capacity was determined from the values of the thermal conductivity, the thermal diffusivity and the bulk density. The values of the heat capacity and the thermal conductivity of the rock samples are reported in Table 2.

The ultrasonic compressional wave velocity and shear wave velocity were measured for using a Punditlab pulse generator delivered by Proceeq® (Chibati *et al.* 2022) in dry and saturated conditions. We used two piezoelectric transducers of 54 and 250 kHz for *P*-wave and *S*-wave acquisitions, respectively. Transducers are pressed against two parallel faces of a core sample (contact gel, depending on the wave-type, was applied to ensure a better connection between the core sample surface and the transducers). The velocity values are reported in Table 2.XXX

3 RELATIONSHIPS BETWEEN PETROPHYSICAL PROPERTIES

In this section, we discuss the relationship between the petrophysical properties and their dependence on two fundamental parameters, namely the connected porosity and the CEC. We propose simple relationships to connect the parameters of interest.

3.1. Archie's law

We first start by discussing the relationship between the intrinsic formation factor F and the connected porosity ϕ, a relationship known in the literature as Archie's law (Archie 1942):

$$F = \phi^{-m}, \tag{3}$$

where m is called the first Archie's exponent or porosity exponent (sometimes the cementation exponent but this inadequate terminology for be forgotten). The fit of Archie's law to our experimental data is shown in Fig. 8. For our data set, we obtain $m = 2.16 \pm 0.02$. As shown in Fig. 8, our data set is consistent with other data sets obtained with core samples from various stratovolcanoes demonstrating again the robustness of this relationship for volcanic rocks. Since there is a lot of confusion in the literature regarding the formation factor, it is worth mentioning that the (intrinsic) formation factor is not the ratio of the pore conductivity by the conductivity of the rock samples (Waxman & Smits 1968). Here again, many studies forget about surface conductivity and use an inappropriate definition for the formation factor. The use of an apparent formation factor defined as the ratio of the resistivity of the rock divided by the resistivity of the pore water leads to inconsistent results (Erikson & Jarrard 1999).

3.2. Surface conductivity normalized chargeability and CEC

We analyse now the relationship between the surface conductivity σ_S (associated with conduction in the electrical double layer) and the CEC. The CEC describes the concentration of exchangeable sites on the mineral surface per unit mass of grains. According to the dynamic Stern layer model, the surface conductivity and the CEC are related to each other by,

$$\sigma_S = \frac{1}{F\phi} B \rho_g \mathrm{CEC}, \tag{4}$$

where F is the formation factor, ϕ the connected porosity, B an effective mobility of the counterions in the double layer coating the surface of the grains [$B(\mathrm{Na}^+, 25\ ^\circ\mathrm{C}) = 3.1 \times 10^{-9}\ \mathrm{m^2 s^{-1}\ V^{-1}}$], ρ_g the mass density of the grains (2700–2900 kg m^{-3}) and CEC denotes the CEC. According to eq. (4), the surface conductivity is therefore proportional to the CEC divided by the bulk tortuosity obtained by the product of the formation factor by the connected porosity.

In Fig. 9, we plot the surface conductivity data versus the independently measured CEC scaled by the tortuosity of the pore space given by the product $F\phi$. As expected, we observe a correlation in agreement with eq. (2), the study of Revil *et al.* (2022), and few additional data set from the literature. This is also consistent with

Table 2. Other physical properties including the dry and water-saturated thermal conductvities, λ_{dry} and λ_{sat}, respectively, the thermal capacity of the dry and water-saturated core samples, C_{pdry} and C_{psat}, respectively, the seismic *P*-wave velocity of the dry and water-saturated core samples, Vp_{dry} and Vp_{sat}, respectively, and finally the shear wave velocity of the saturated core sample, V_{Ssat}.

Full name	λ_{dry} (W m^{-1} K^{-1})	C_{pdry} (kJ kg^{-1} K^{-1})	λ_{sat} (W m^{-1} K^{-1})	C_{psat} (kJ kg^{-1} K^{-1})	Vp_{dry} (m s^{-1})	Vp_{sat} (m s^{-1})	V_{Ssat} (m s^{-1})
GD15_01	1.6550	0.85600	1.7000	0.77500	4484.0	4965	2129
GD15_03	0.93900	0.89100	-	-	2416.0	-	1225
GD15_06	0.96300	0.92900	-	-	1751.0	-	-
GD15_07	0.73600	0.95800	-	-	1697.0	-	1438
GD15_09	0.60700	0.82500	-	-	1697.0	-	516
GD15_106	1.8840	0.82000	1.8750	0.69900	6233.0	5295	2830
GD15_112	0.41600	1.1160	-	-	1555.0	-	926
GD15_124	-	-	-	-	-	-	-
GD15_130	0.52200	1.1790	-	-	2306.0	-	1182
GD15_138	1.1790	0.92300	-	-	2379.0	-	1334
GD15_15	1.0020	0.82600	-	-	3584.0	-	1701
GD15_150	0.89700	0.90800	1.4540	0.94400	2891.0	3341	1486
GD15_151	1.8060	0.71600	-	-	3623.0	-	1937
GD15_152	1.8780	0.73600	1.8100	0.65300	5638.0	5858	3448
GD15_154	0.51500	0.77100	-	-	2273.0	-	1109
GD15_160	-	-	-	-	-	-	-
GD15_162	1.7200	0.71000	1.5190	0.41500	5021.0	5651	2705
GD15_164	1.8670	0.75000	1.8560	0.69400	5227.0	5260	2557
GD15_166	1.8090	0.73400	1.8530	0.64000	5023.0	5672	2759
GD15_19	0.49900	0.96600	-	-	2093.0	-	1208
GD15_23	1.3090	0.81200	1.6200	0.57500	4233.0	4843	2554
GD15_26	1.4070	0.82000	1.7140	0.70500	4152.0	4829	2405
GD15_35	0.87200	0.98400	1.4520	1.0570	1412.0	939	-
GD15_36	1.7400	0.99500	1.7770	0.70900	5142.0	5569	2769
GD15_37	1.8750	0.90900	1.8730	0.70400	4926.0	5155	2411
GD15_40	1.3070	0.83300	1.3570	0.44500	3450.0	4039	1989
GD16_03	1.5480	0.86400	2.2220	1.1030	1837.0	1486	872
GD16_05	2.0180	0.62500	2.6250	0.92600	2660.0	2999	1702
GD16_08	1.3570	0.70400	-	-	3330	-	1898
GD16_09	1.2580	0.76600	-	-	2898	-	1601
GD16_10	0.84900	1.6220	-	-	790	-	-
GD16_13	0.74900	0.75300	-	-	2180	-	1054
GD16_16	0.34200	0.63300	-	-	1465	-	878
GD16_18	0.58800	0.93100	-	-	2528	-	1397
GD16_19	0.60000	0.79500	-	-	1800	-	936
GD16_23	0.66200	0.91300	-	-	1871	-	1318
GD16_26	0.51500	0.78700	-	-	1511	-	914.
GD17_09	1.0440	0.93100	-	-	3164	-	1795
GD17_12	0.92800	0.87200	-	-	2055	-	1243
GD17_13	1.0820	0.90100	-	-	2215	-	1178
GD17_80	-	-	-	-	-	-	-

the results shown in Fig. 7(b) where the conductivity ratio σ'/σ_w depends on the ratio $CEC/\phi\sigma_w$ (as expected from eqs 1 and 4).

The normalized chargeability (obtained here by fitting the complex conductivity spectra with a Cole–Cole model, see Revil *et al.* 2022, for a detailed description of the methodology) can be directly related to the quadrature conductivity as discussed in details in Revil *et al.* (2017a, b) and references therein (see Fig. 10). The Cole–Cole normalized chargeability can be related to the CEC according to (Revil *et al.* 2022),

$$M_n = \frac{1}{F\phi}\lambda\rho_g CEC, \tag{5}$$

where λ is another effective mobility related to the double layer [$\lambda(Na^+, 25\ ^\circ C) = 3.0 \pm 0.7 \times 10^{-10}$ m^{2}s^{-1} V^{-1}, see Revil 2013; Revil *et al.* 2017a, 2022 for details]. It follows that the surface conductivity can be related to the normalized chargeability by (Revil 2013; Revil *et al.* 2017a, 2022),

$$\frac{M_n}{\sigma_S} = \frac{\lambda}{B} \equiv R = 0.09, \tag{6}$$

where R is a universal dimensional parameter independent of temperature and saturation or textural properties. The proportionality between the surface conductivity and the normalized chargeability is demonstrated in Fig. 11, checking in passing the value of the dimensionless parameter R.

As a side note the apparent mobilities B and λ are related to the intrinsic mobilities of the counterions in the Stern and diffuse layers by $B = \beta_{(+)}(1-f) + \beta^S_{(+)}f$ and $\lambda = \beta^S_{(+)}f$, where f (dimensionless) denotes the partition coefficient (fraction of counterions in the Stern layer versus the entire double layer), $\beta_{(+)}$ denotes the mobility of counterions in diffuse layer, and $\beta^S_{(+)}$ describes the mobility of the counterions in the Stern layer (see Revil *et al.* 2017c).

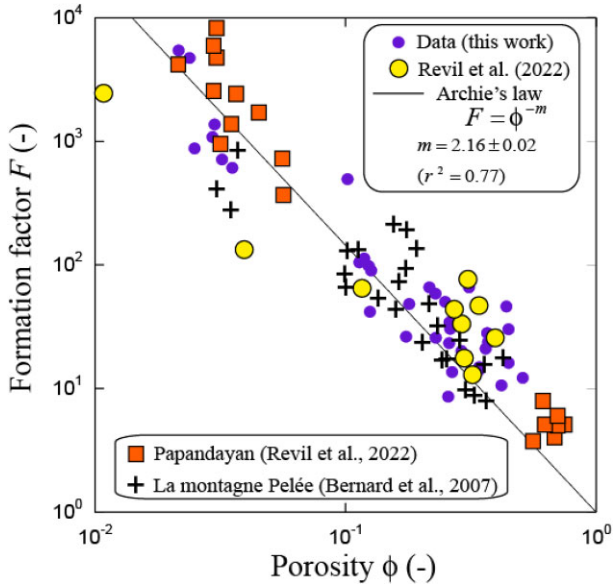

Figure 8. Relationship between the formation factor and the connected porosity using Archie's law in stratovolcanoes. Fit of Archie's law for the data set developed in this work for La Soufrière de la Guadeloupe volcano. We have also provided the data from the recent study of Revil *et al.* (2022) using 10 additional core samples from the same volcano and core samples data from another stratovolcano, Papandayan in Indonesia, from the study of Revil *et al.* (2022). The data from La Montagne Pelée volcano (Martinique Island, France) are from Bernard *et al.* (2007) with the exception of the pumices.

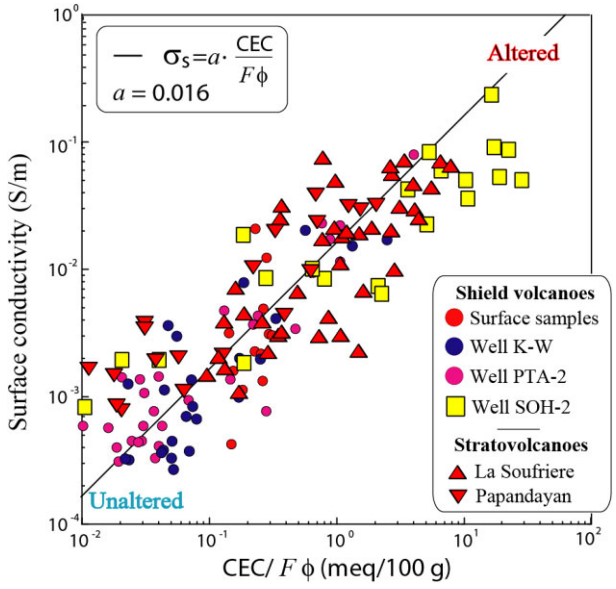

Figure 9. Dependence of surface conductivity on CEC in stratovolcanoes. Surface conductivity (S m^{-1}) versus the ratio CEC/$F\phi$, where CEC denotes the cation exchange capacity [in meq (100 g)$^{-1}$], F the formation factor and ϕ the porosity [1 meq (100 g)$^{-1}$ = 963.2 C kg^{-1}]. There are 135 samples in the plot including the 41 samples from this study. The slope is equal to $B\,\rho_g$. A comparison is done with various data set from Kilauea shield volcano (Hawaii).

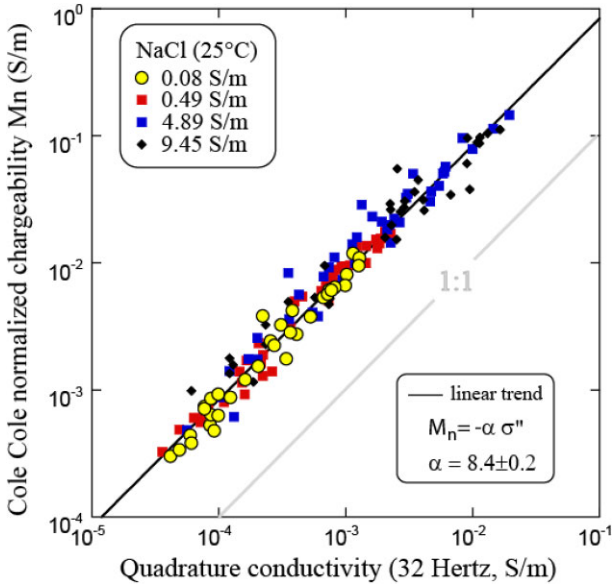

Figure 10. Cole–Cole normalized chargeability versus quadrature conductivity (at 32 Hertz) for la Soufrière stratovolcano. The fit of the data performed over the entire salinity data set ($r^2 = 0.96$, 4 salinities) is consistent with the results recently obtained by Revil *et al.* (2022) for the slope, which is, according to the theory, universal.

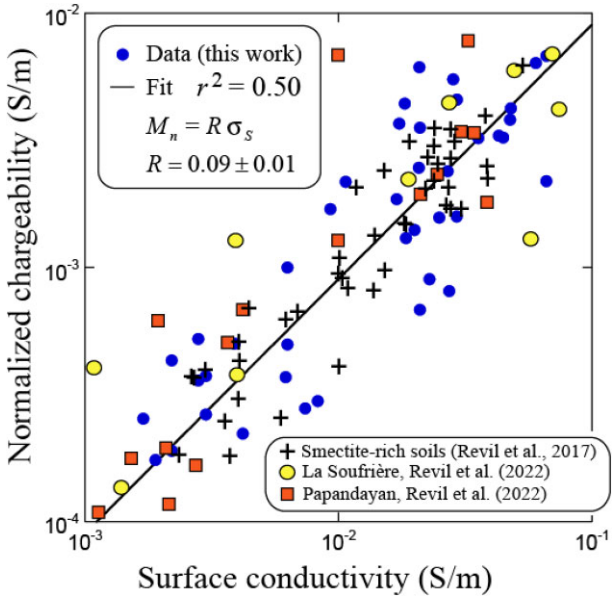

Figure 11. Relationship between the normalized chargeability (from a Cole–Cole fit of the data at the lowest salinity $\sigma_w = 0.08$ S m^{-1}, NaCl at 25 °C, see Revil *et al.* 2022, for the methodology) and the surface conductivity σ_S. The ratio between the two parameters is equal to the dimensionless parameter $R = \lambda/B = 0.09 \pm 0.01$. We also added the data from La Soufrière and Papandayan stratovolcanoes from the recent study of Revil *et al.* (2022) (M_n obtained at salinity $\sigma_w = 0.10$ S m^{-1} at 25 °C, NaCl) as well as the data from the study of Revil *et al.* (2017c) for smectite-rich soils (Cole–Cole normalized chargeability).

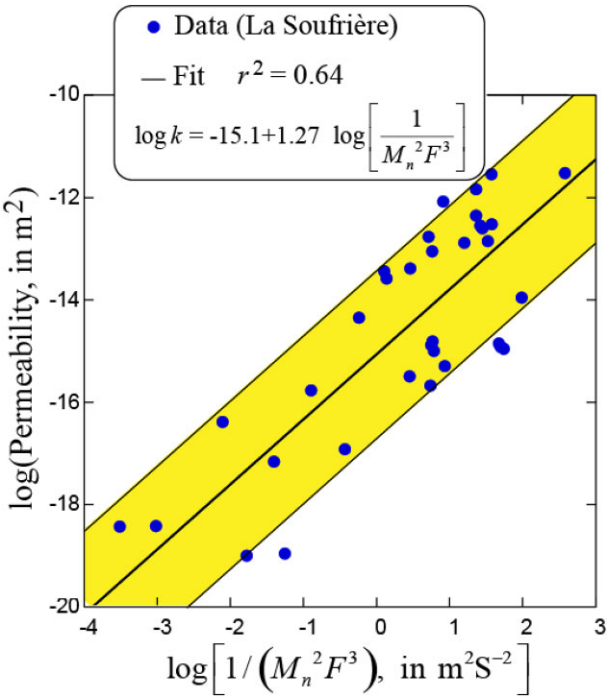

Figure 12. Relationship between the permeability k and the Cole–Cole normalized chargeability (at the lowest salinity) and the formation factor F. The permeability data covers 7 orders of magnitude.

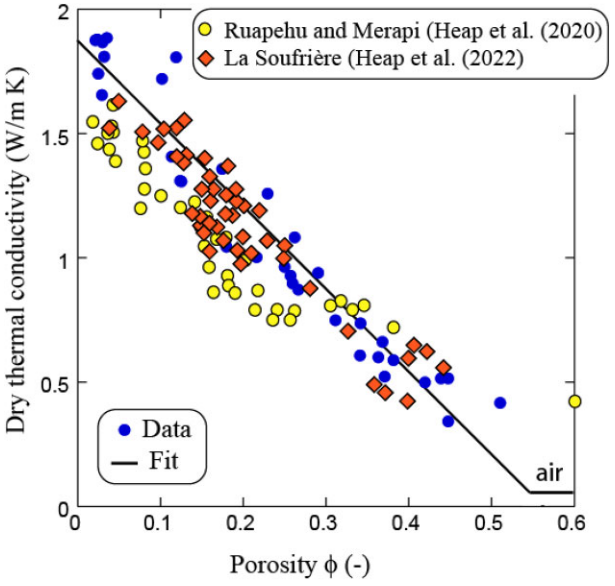

Figure 13. Dry thermal conductivity versus connected porosity. Note that the thermal conductivity of air is 0.024 W m^{-1} K^{-1}. The plain line corresponds to a fit with the equation described in the main text. A comparison is made with the data set reported by Heap *et al.* (2020) for Merapi (Indonesia) and Ruapehu (New Zealand) volcanoes (andesites).

3.3. Permeability, formation factor and CEC

The permeability can be connected to an effective porosity related itself to the formation factor and to a pore size. In turn, the pore size can be related to the surface conductivity and the normalized chargeability (Revil 2013). Scaling relationships imply that the scaling between the permeability k and the formation factor and the normalized chargeability should be, $k = b/(M_n^2 F^3)$ where

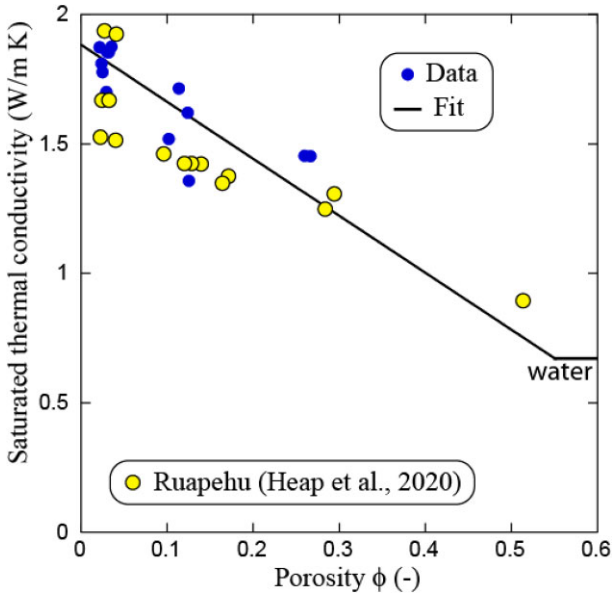

Figure 14. Water-saturated thermal conductivity versus connected porosity. Note that the thermal conductivity of water is 0.63 W m^{-1} K^{-1}. The plain line corresponds to a fit with the equation described in the main text. For comparison, we have also added the data from Ruapehu volcano (New Zealand) from Heap *et al.* (2020) (water-saturated).

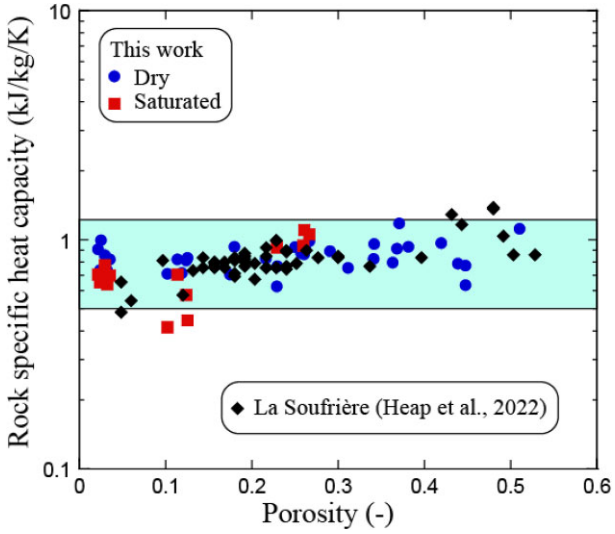

Figure 15. Specific heat capacity of the (dry and water-saturated) rock samples versus the connected porosity. A similar plot can be obtained when plotted as a function of the CEC. We have added for comparison, the data from Heap *et al.* (2022a, b) from La Soufrière volcano. At first approximation, the specific heat capacity is quite independent of both the porosity and CEC (we note a small increase with the porosity). The averaged heat capacity is 0.90 ± 0.30 kJ^{-1} kg^{-1} K^{-1}.

b is a fitting constant. In Fig. 12, we fit the data with the following empirical relationship:

$$\log k = -15.1 + 1.27 \log\left(M_n^2 F^3\right). \quad (7)$$

We obtain a fair correlation ($r^2 = 0.64$), which will need to be confirmed by additional data sets in future investigations. It follows that induced polarization can be used to infer the permeability of the rock matrix inside approximately more or less two orders of magnitude.

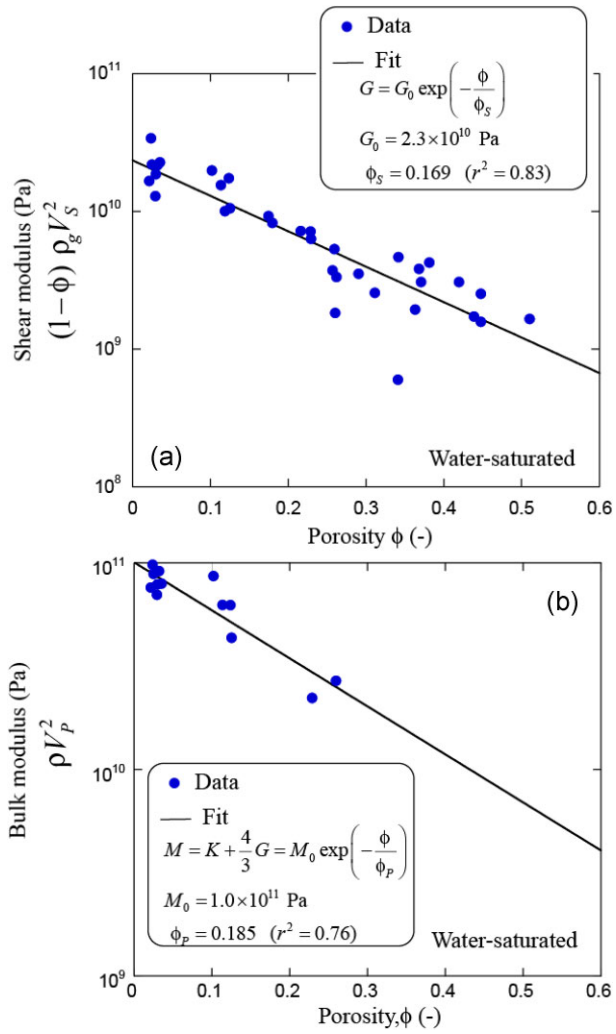

Figure 16. Influence of the porosity upon the shear wave velocity and the *P*-wave velocity. (a) *P*-wave analysis at saturation. The quantity G_0 corresponds to the shear modulus of the solid phase. (b) Shear-wave analysis at saturation. K and G are the bulk and shear moduli, respectively, whereas M is the modulus for the *P*-wave velocity. The quantity M_0 corresponds to the modulus of the solid phase.

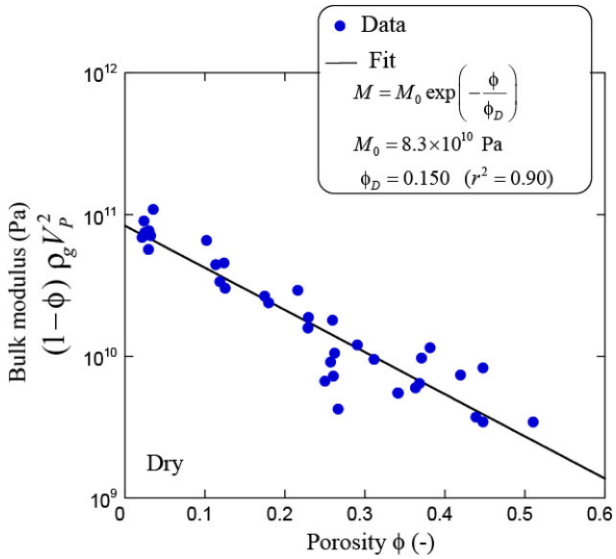

Figure 17. Influence of the porosity upon the *P*-wave velocity in dry state conditions. The quantity M_0 corresponds to the modulus of the solid phase.

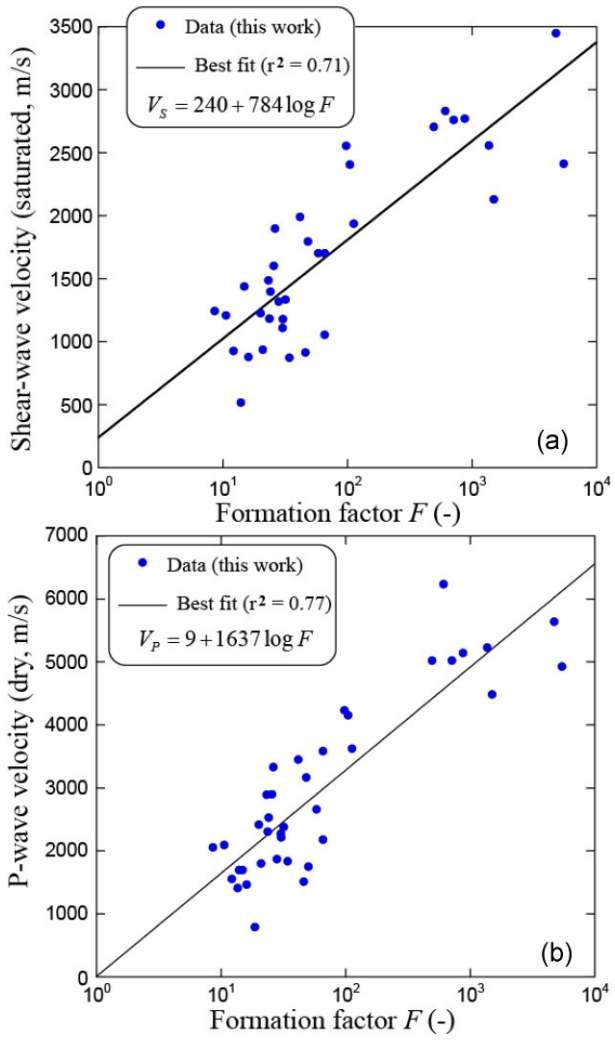

Figure 18. Relationships between the seismic velocity and the formation factor for La Soufrière volcano. (a) Relationship between the S-wave velocity and the formation factor. (b) Relationship between the *P*-wave velocity and the formation factor.

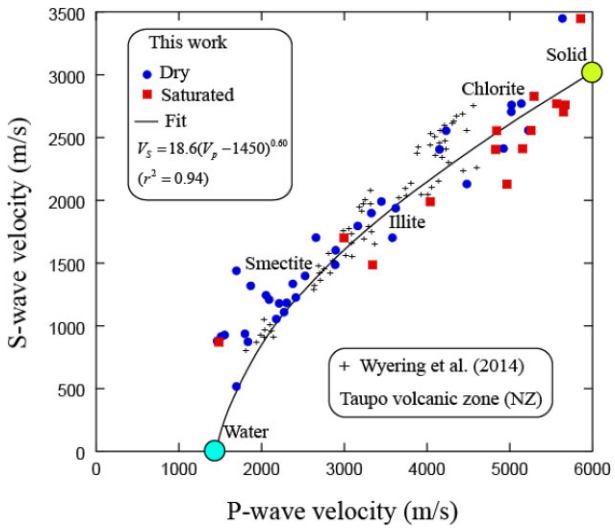

Figure 19. Shear versus compressional wave velocity. We have also added for comparison purpose the data from Wyering *et al.* (2014) using samples from the Taupo volcanic zones (NZ, New Zealand) with the alteration facies rich in smectite, illite and chlorite. Note that the relationship between the two properties cannot be linear as assumed by Wyering *et al.* (2014) except if the first point (for water) is not used in the analysis. The plot implies for instance that the clay cap is a low-velocity area.

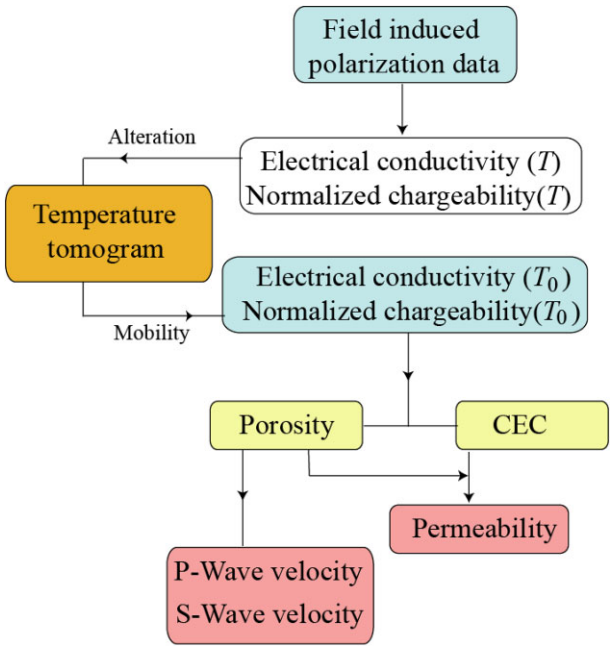

Figure 20. Flow chart to compute seismic tomograms of a volcano from an induced polarization survey. The flow chart is showing how we can use the relationships developed in this study to transform an induced polarization tomogram into seismic wave tomograms.

3.4. Thermal conductivity

The thermal conductivity data are plotted as a function of the (connected) porosity in Fig. 13 for the dry case and in Fig. 14 for the water-saturated case. We have added additional data from the literature using core samples from various stratovolcanoes. In all cases, the data obey approximately a linear relationship between the thermal conductivity and the porosity. The thermal conductivity of the volcanic rock samples can be therefore fitted by a linear relationship taking the following form

$$\lambda = \begin{cases} \lambda_S \left(1 - \frac{\phi}{\phi_C}\right) + \lambda_f \frac{\phi}{\phi_C}, \text{for } 0 \le \phi \le \phi_C \\ \lambda_f, \text{for } \phi_C \le \phi \le 1 \end{cases} \quad (8)$$

For the dry samples used in this paper (Fig. 13), we have $\lambda_f = 0.024$ W m^{-1}K^{-1} (thermal conductivity of air), a critical porosity of $\phi_c = 0.55$ and $\lambda_S = 1.8$ W m^{-1} K^{-1} (thermal conductivity of the solid phase). The same parameters can be used for the water-saturated case (Fig. 14) with $\lambda_f = 0.63$ W m^{-1} K^{-1} (thermal conductivity of liquid water) and the same 2 other parameters ($\phi_c = 0.55$ and $\lambda_S = 1.8$ W m^{-1}K^{-1}). The critical porosity is the porosity value at which the thermal conductivity of the rock is equal to the thermal conductivity of the pore fluid. In this paper, we do not investigate the effect of partial saturation (see Jougnot & Revil 2010).

The thermal conductivity of the solid phase can be compared to the thermal conductivity of some minerals like plagioclase ($\lambda_S = 1.9 \pm 0.4$ W m^{-1} K^{-1}), biotite ($\lambda_S = 2.3 \pm 0.2$ W m^{-1} K^{-1}), smectite ($\lambda_S = 1.9 \pm 0.2$ W m^{-1} K^{-1}), illite ($\lambda_S = 1.9$ W m^{-1}K^{-1}), chabazite (zeolite, $\lambda_S = 1.2 \pm 0.4$ W m^{-1} K^{-1}, see Revil 2000, and references therein). The difference between the different sets of samples could be due to slight variations of the petrographic compositions. The dry thermal conductivity values at 0 per cent of porosity are significative of these petrographic compositions. The main regression lines present similar λ_S significative of the petrographic of the core samples but we let this subtle effect on the side here.

3.5. Specific heat capacity

The specific heat capacity data (obtained from the thermal diffusivity and the thermal conductivity data) are plotted as a function of the porosity in Fig. 15. The data show a very slight increase of the values with the connected porosity around a mean value of 0.90 ± 0.30 kJ kg^{-1} K^{-1} (see also Heap *et al.* 2020, 2022a,b). For practical applications, we can consider that the specific heat capacity is constant, independent of both porosity and alteration.

3.6. Seismic velocities

The seismic velocity data are plotted as a function of the porosity in Figs 16 and 17. Since the velocity depends on the mechanical moduli and the density, we plot the product of the density by the velocity squared as a function of the connected porosity. The data shown in Figs 16 and 17 demonstrate a high level of correlation with the connected porosity. For the *S*-wave velocities V_s, the shear modulus is given by

$$G = (1 - \phi)\rho_g V_S^2. \quad (9)$$

We fit the shear modulus data such obtained with the following relationship;

$$G = G_0 \exp\left(-\frac{\phi}{\phi_S}\right). \quad (10)$$

For the shear wave velocity data, we obtain $\phi_S = 0.17$ and the shear modulus of the solid phase $G_0 = 2.3 \times 10^{10}$ Pa (see fit in Fig. 16a). This value can be compared to the shear modulus of plagioclase (3.5×10^{10} Pa, Pabst *et al.* 2015) and smectite (in the range 0.7 to 2.5×10^{10} Pa, For the *P*-wave velocity V_P in saturated conditions, a similar analysis (Fig. 16b), we have for the *P*-wave modulus,

$$M = \rho V_P^2, \quad (11)$$

$$M = M_0 \exp\left(-\frac{\phi}{\phi_P}\right). \quad (12)$$

The best fit yields $\phi_P = 0.19$ and the modulus of the solid phase is given by $M_0 = 1.0 \times 10^{11}$ Pa (Fig. 16b). For the dry *P*-wave velocity (Fig. 17), we have

$$M_{\text{dry}} = (1 - \phi)\rho_g V_P^2, \quad (13)$$

$$M_{\text{dry}} = M_0 \exp\left(-\frac{\phi}{\phi_D}\right), \quad (14)$$

with $\phi_D = 0.15$ and $M_0 = 0.83 \times 10^{11}$ Pa (modulus of the solid phase). As expected, the modulus M_0 does not depend on the state of saturation. The three critical porosity entering eqs (10), (12) and (14) are nearly the same with a critical porosity given as $\phi_C = 0.17 \pm 0.02$.

In Fig. 18, we plot the shear and compressional wave velocity as a function of the formation factor. We observe a fair correlation between the seismic velocities and the log of the formation factor. We can use these relationships to determine directly the *P*- and *S*-wave velocities from the determination of the formation factor itself determined from induced polarization data. Finally, in Fig. 19, we show that the *P*-wave and *S*-wave velocities are strongly related to each other for volcanic rocks.

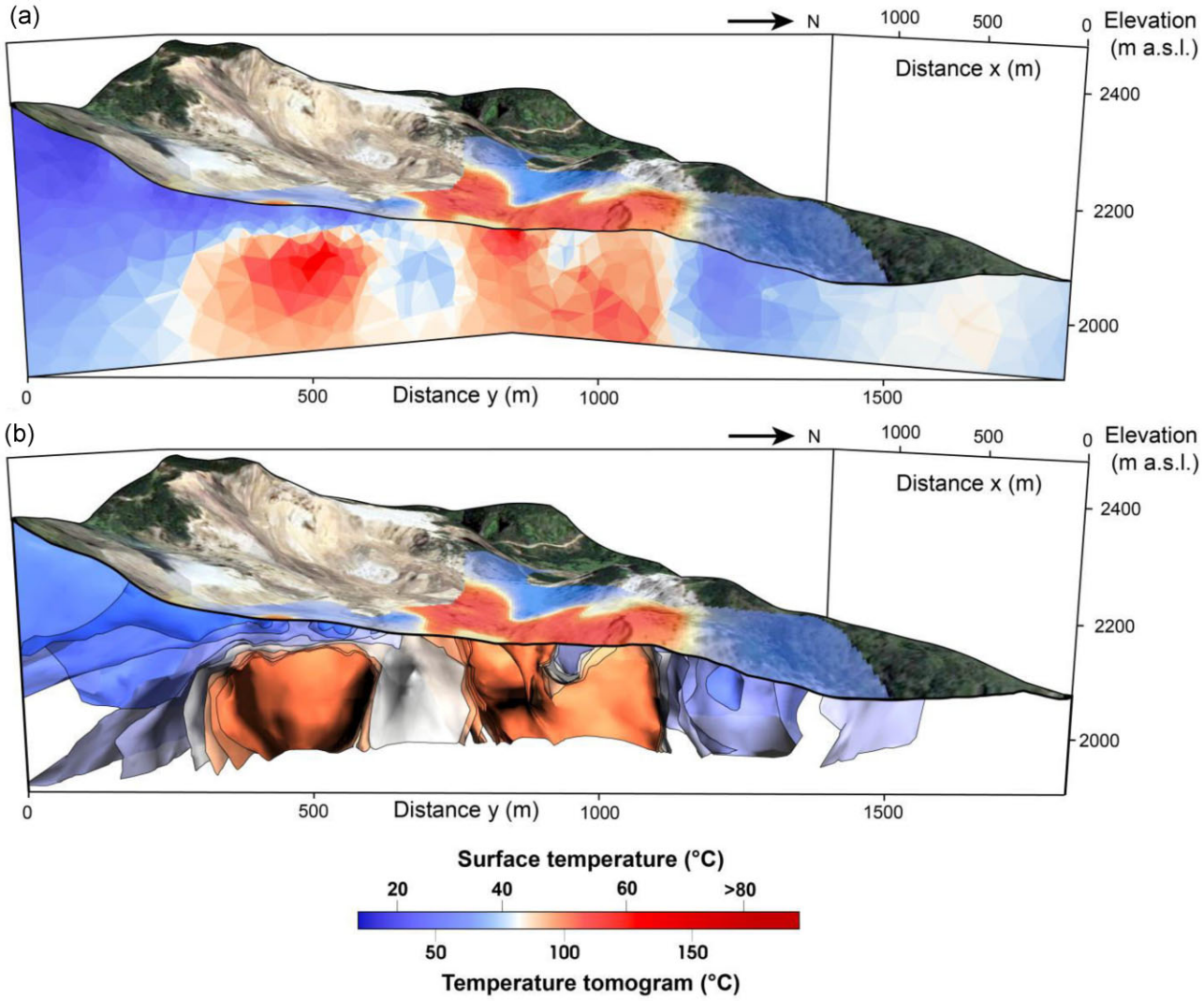

Figure 21. Tomogram of the temperature obtained from the induced polarization measurements. (a) Cross-section. (b) Figure showing the isotherms in 3-D. For the two figures, a comparison can be made with the surface temperature data.

4 FROM INDUCED POLARIZATION TO SEISMIC *P*- AND *S*-WAVE TOMOGRAMS

In this section, we discuss how we can convert an induced polarization survey into a tomogram of the seismic velocities. In our opinion, this is the first step in performing in the future joint inversion of electrical and seismic data on active volcanoes. The flow chart we follow is shown in Fig. 19. We first perform an induced polarization survey used to image the in-phase conductivity and the normalized chargeability. Then, we perform a temperature tomogram using the procedure described by Revil *et al.* (2022).

Assuming Archie's law with $m = 2$ to simplify a bit the relationships, the conductivity and the normalized chargeability as,

$$\sigma' = \phi^2 \sigma_{\rm w} + \phi B \rho_g \mathrm{CEC}, \tag{15}$$

$$M_n = \phi \lambda \rho_g \mathrm{CEC}. \tag{16}$$

If the pore water conductivity is known, we have two unknowns to determine, the CEC and the porosity. So once a tomogram of the conductivity and normalized chargeability is obtained, we can determine cell-by-cell the porosity and the CEC using the following relationships,

$$\phi = \sqrt{\frac{\sigma' - M_n/R}{\sigma_{\rm w}}}, \tag{17}$$

$$\mathrm{CEC} = M_n/\phi\lambda\rho_g. \tag{18}$$

For eq. (18), a small temperature correction for λ is required using the temperature tomogram and according to $\lambda(T) = \lambda(T_0)(1 + \alpha(T - T_0))$ with $\alpha = 0.02\,(^\circ\mathrm{C})^{-1}$ and $(\lambda(\mathrm{Na}^+, T_0 = 25\ ^\circ\mathrm{C}) = 3.0 \pm 0.7 \times 10^{-10}\ \mathrm{m^2 s^{-1} V^{-1}}$. Then, we can compute the *P*-wave velocity according to

$$V_P = \sqrt{\frac{M_0 \exp\left(-\frac{\phi}{\phi_P}\right)}{(1-\phi)\rho_g + \phi\rho_f}}, \tag{11}$$

with $\phi_P = 0.19$ and $M_0 = 1.0 \times 10^{11}$ Pa, $\rho_g = 2900\ \mathrm{kg\ m^{-3}}$ and $\rho_f = 1000\ \mathrm{kg\ m^{-3}}$. V_S is then computed from the *P*-wave velocity (see relationship in Fig. 20).

We apply the previous transforms to the Papandayan stratovolcano located in Java Island (Indonesia). Papandayan (2665 masl, metres above sea level) volcano is an andesitic stratovolcano in

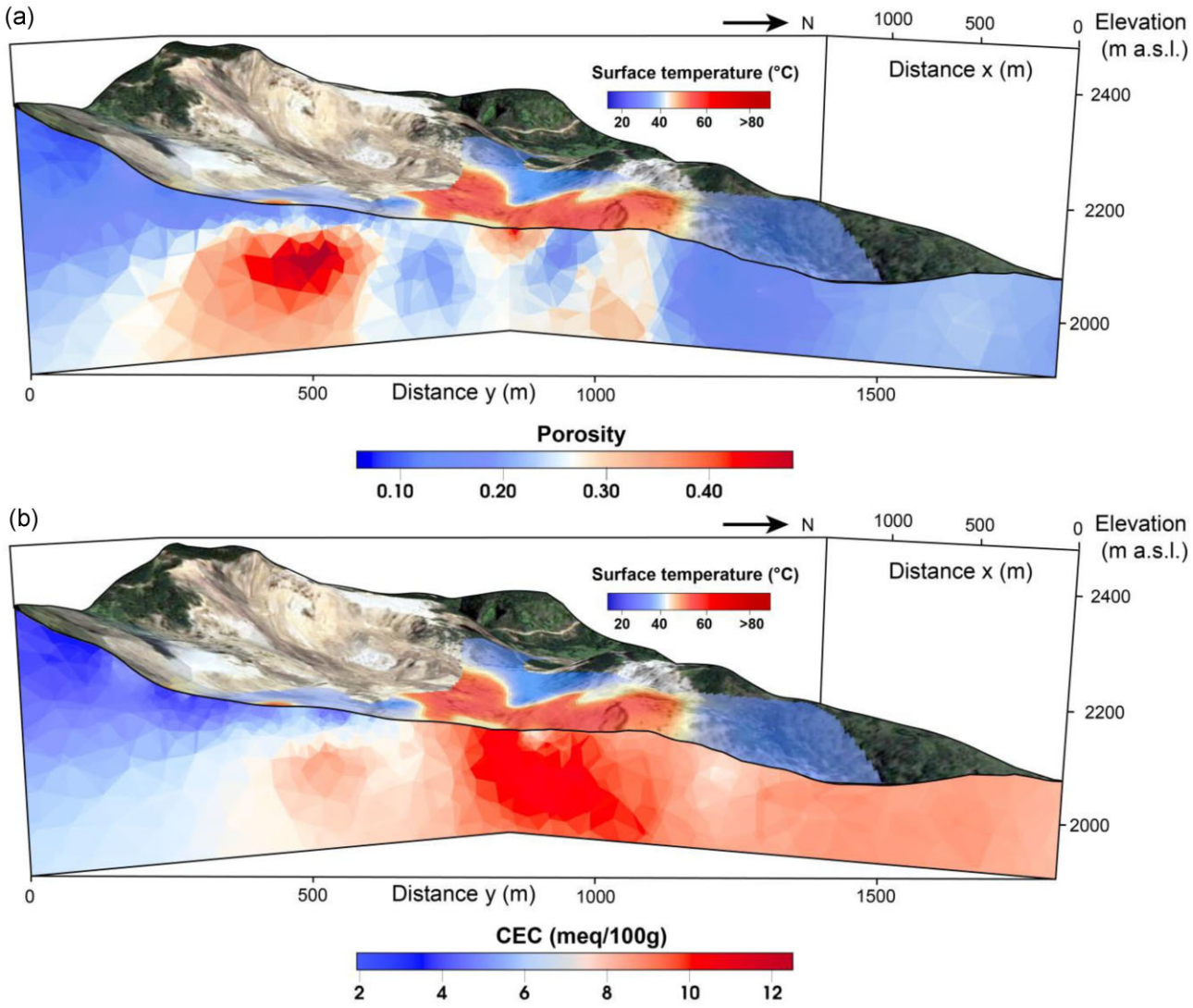

Figure 22. Porosity and cation exchange capacity (CEC) tomograms obtained from the induced polarization tomogram according to the flow chart shown in Fig. 20. (a) Porosity tomogram. (b) CEC tomogram. The high CEC subvolume reflects the high degree of alteration below the surface area characterized by a high temperature.

Western Java Island in Indonesia (Syahbana *et al.* 2014). This volcano is characterized by an intense hydrothermal activity. This activity is evidenced by sulfate mud pools, fumaroles and gas emission, and four active vents (the Mas, Manuk, Nangklak and Baru craters). An induced polarization survey was performed in 2018. At Papadayan, five resistivity/induced polarization profiles were acquired in the 1772 crater of this stratovolcano (Revil *et al.* 2022). Each profile is characterized by 48 electrodes with an electrode spacing of 30 m. The survey was acquired with a Czech ARES II instrument using a Wenner-alpha array and a window of 100 ms (from 105 to 205 ms after shutting down the primary current) for the chargeability. The survey includes 240 electrodes and 1800 apparent resistivity and chargeability data. In addition, a Digital Elevation Map was used to build the geometry of the ground surface. We use a conductivity of the pore water of 1 S m^{-1} at 25 °C from the high conductivity of the Spring that are present here.

The temperature tomogram obtained from the induced polarization data is shown in Fig. 21 (see Revil *et al.* 2022). The results can be compared to the ground surface temperature data obtained from remote-sensing analysis (see details in Revil *et al.* 2022). Then, the induced polarization data are corrected for the temperature effect on the ionic mobilities and we obtained the porosity and CEC tomograms shown in Fig. 22. The porosity ranges from 5 to 50 per cent whereas the CEC ranges from 2 to 12 meq $(100\ g)^{-1}$, both being realistic ranges. In Table 2, the porosity ranges from 2 to 51 per cent and the CEC from 2 to 35 meq $(100\ g)^{-1}$. Finally, these data are converted to *P*- and *S*-wave velocity tomograms shown in Fig. 23. These tomograms could be used as a prior model to better localize seismic source events and refine the velocity model through seismic wave tomography.

5 CONCLUSIONS

We have developed a new data set of experimental data for 41 rock samples from la Soufrière stratovolcano in Guadeloupe Island (France). First, we analysed the relationship from the geoelectrical parameters determined from the complex conductivity spectra obtained in the frequency range 10 mHz–45 kHz. We show

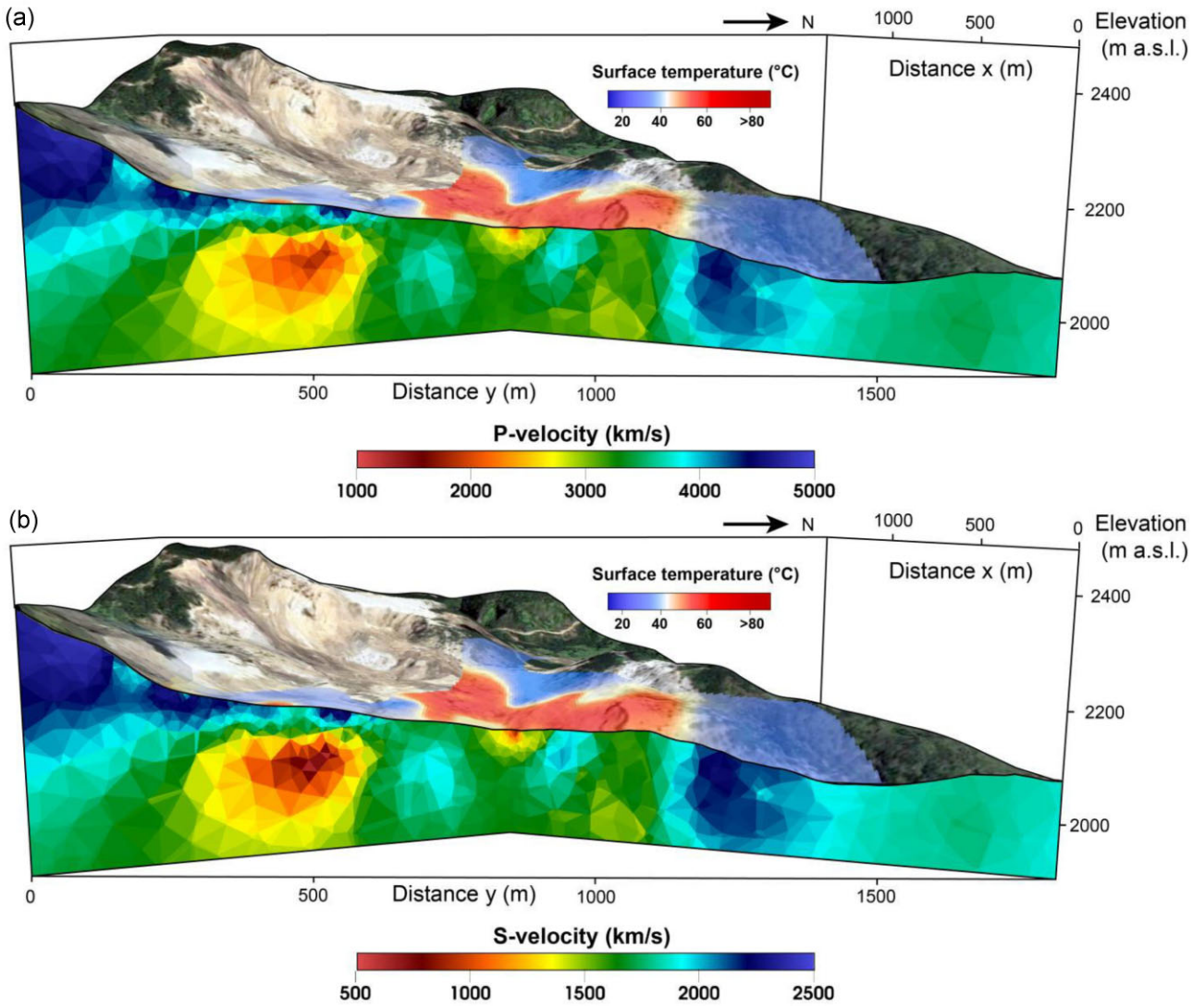

Figure 23. Seimic velocity tomograms. (a) Compressional (*P*-)wave velocity tomogram. (b) Shear (*S*-)wave tomogram. These tomograms come from the flow chart shown in Fig. 20 using the porosity as input parameter.

that the formation factor can be related to the connected porosity via Archie's law and that surface conductivity and normalized chargeability can be related to the porosity, formation factor and CEC.

Then, we show that permeability, thermal conductivity and seismic velocities can be derived from the CEC and the porosity or directly from the geoelectrical parameters from induced polarization. As an example of application of our methodology, we transform a 3-D tomography of induced polarization into a seismic *P*-wave velocity tomogram, which could be used to start a seismic tomography from passive seismic data. By analysing both types of data in combination, we expect to gain a more comprehensive understanding of the internal dynamics of stratovolcanoes and the factors that influence their activity.

DATA AVAILABILILY

The data used in this paper are available upon request to the corresponding author. There is one statement clearly stated above.

ACKNOWLEDGMENTS

We thank the CNRS for supporting this work. We acknowledge H. Grandis and the Volcanological Survey of Indonesia (PVMBG) for permission to use the data from Papandayan Volcano. Sampling and some petrophysical characterization of the Soufrière volcano are supported by the GEOTREF program. Kai Zhang would also thank the founding from China Scholarship Council. We thank Egon Zimmerman for the construction of the ZELSIP04-V02 impedance meter. We thank the two referees, K. Titov and an anonymous referee, and the editor for their useful comments and their time.

REFERENCES

Anovitz, L.M. & Cole, D.R., 2015. Characterization and analysis of porosity and pore structures, *Rev. Mineral. Geochem.,* **80,** 61–164.

Aran, D., Maul, A. & Masfaraud, J., 2008. A spectrophotometric measurement of soil cation exchange capacity based on cobaltihexamine chloride absorbance, *C.R. Geosci.,* **340**(12), 865–871.

Archie, G.E., 1942. The electrical resistivity log as an aid in determining some reservoir characteristics, *Trans. AIME,* **146,** 54–62.

Bernard, M.-L., Zamora, M., Géraud, Y. & Boudon, G., 2007. Transport properties of pyroclastic rocks from Montagne Pelée volcano (Martinique, Lesser Antilles), *J. geophys. Res.,* **112**(B5), doi:10.1029/2006JB004385.

Bonafede, M., 1991. Hot fluid migration: an efficient source of ground deformation: application to the 1982–1985 crisis at Campi Flegrei-Italy, *J. Volc. Geotherm. Res.,* **48**(1–2), 187–198.

Boulanouar, A., Rahmouni, A., Boukalouch, M., Samaouali, A., Geraud, Y., Harnafi, M. & Sebbani, J., 2013. Determination of thermal conductivity and porosity of building stone from ultrasonic velocity measurements, *Geomaterials,* **3,** 138–144.

Carbonari, R., Di Maio, R. & Piegari, E., 2019. Feasibility to use continuous magnetotelluric observations for monitoring hydrothermal activity. Numerical modeling applied to Campi Flegrei volcanic System (Southern Italy), *Front. Earth Sci.,* **7,** doi:10.3389/feart.2019.00262.

Chibati, N., Géraud, Y. & Essa, K.S., 2022. Petrophysical characterization and thermal conductivity prediction of serpentinized peridotites, *Geophys. J. Int.,* **231**(3), 1786–1805.

Chiou, C.T. & Rutherford, D.W., 1997. Effects of exchanged cation and layer charge on the sorption of water and EGME vapors on Montmorillonite clays, *Clays Clay Miner.,* **45**(6), 867–880.

Erikson, S.N. & Jarrard, R. D., 1999. Porosity-formation factor and porosity-velocity relationships in Barbados prism, *J. geophys. Res.,* **104**(B7), 15 391–15 407.

Favier, A., Lardeaux, J.-M., Corsini, M., Verati, C., Navelot, V., Géraud, Y. & Voitus, E., 2021. Characterization of an exhumed high-temperature hydrothermal system and its application for deep geothermal exploration: an example from Terre-de-Haut Island (Guadeloupe archipelago, Lesser Antilles volcanic arc), *J. Volc. Geotherm. Res.,* **418,** 107256.

Feuillet, N., Manighetti, I. & Tapponnier, P. 2001. Extension active perpendiculaire à la subduction dans l'arc des Petites Antilles (Guadeloupe, Antilles françaises), *Comptes Rendus de l'Academie de Sciences - Serie IIa: Sciences de la Terre et des Planetes,* **333,** 583–590.

Finizola, A. *et al.*, 2006. Hydrogeological insights at Stromboli volcano (Italy) from geoelectrical, temperature, and CO_2 soil degassing investigations, *Geophys. Res. Lett.,* **33**(17), doi:10.1029/2006GL026842.

Fournier, N. & Chardot, L., 2012. Understanding volcano hydrothermal unrest from geodetic observations: insights from numerical modeling and application to White Island volcano, New Zealand, *J. geophys. Res.,* **117**(11), 1–16.

Gola, G. *et al.*, 2021. A novel multidisciplinary approach for the thermo-rheological study of volcanic areas: the case study of Long Valley Caldera, *J. geophys. Res.,* **126**(2), e2020JB020331, doi:10.1029/2020JB020331.

Gottsmann, J., Camacho, A.G., Martí, J., Wooller, L., Fernández, J., García, A. & Rymer, H., 2008. Shallow structure beneath the Central Volcanic Complex of Tenerife from new gravity data: implications for its evolution and recent reactivation, *Phys. Earth planet. Inter.,* **168**(3–4), 212–230.

Gottsmann, J., Flynn, M. & Hickey, J., 2020. The transcrustal magma reservoir beneath Soufrière Hills volcano, Montserrat: insights from 3-D geodetic inversions, *Geophys. Res. Lett.,* **47**(20), 1–10.

Haffen, S., Géraud, Y., Rosener, M. & Diraison, M., 2017. Thermal conductivity and porosity maps for different materials: a combined case study of granite and sandstone, *Geothermics,* **66**, 143–150.

Heap, M.J. *et al.*, 2020. The thermal properties of porous andesite, *J. Volc. Geotherm. Res.,* **398,** doi:10.1016/j.jvolgeores.2020.106901.

Heap, M.J. *et al.*, 2022a. The thermal properties of hydrothermally altered andesites from La Soufrière de Guadeloupe (Eastern Caribbean), *J. Volc. Geotherm. Res.,* **421,** doi:10.1016/j.jvolgeores.2021.107444.

Heap, M.J., Meyer, G.G., Noel, C., Wadsworth, F.B., Baud, P. & Violay, M.E.S., 2022b. The permeability of porous volcanic rock through the brittle-ductile transition, *J. geophys. Res.,* **127**(6), e2022JB024600. doi:10.1029/2022JB024600.

Hill, G. J. *et al.*, 2020. Temporal magnetotellurics reveals mechanics of the 2012 Mount Tongariro, NZ, eruption, *Geophys. Res. Lett.,* **47,** e2019GL086429, doi:10.1029/2019GL086429.

Iwamori, H. *et al.*, 2021. Simultaneous analysis of seismic velocity and electrical conductivity in the crust and the uppermost mantle: a forward model and inversion test based on grid search, *J. geophys. Res.,* **126**(9), doi:10.1029/2021JB022307.

Jardani, A. & Revil, A., 2009. Stochastic joint inversion of temperature and self-potential data, *Geophys. J. Int.,* **179**(1), 640–654.

Jasim, A., Whitaker, F.F. & Rust, A.C., 2015. Impact of channelized flow on temperature distribution and fluid flow in restless calderas: insight from Campi Flegrei caldera, Italy, *J. Volc. Geotherm. Res.,* **303,** 157–174.

Jougnot, D., Ghorbani, A., Revil, A., Leroy, P. & Cosenza, P., 2010. Spectral induced polarization of partially saturated clay-rocks: a mechanistic approach, *Geophys. J. Int.,* **180**(1), 210–224.

Jougnot, D. & Revil, A., 2010. Thermal conductivity of unsaturated clay-rocks, *Hydrol. Earth Syst. Sci.,* **14,** 91–98.

Karaoulis, M., Revil, A., Minsley, B., Todesco, M., Zhang, J. & Werkema, D.D., 2014. Time-lapse gravity inversion with an active time constraint, *Geophys. J. Int.,* **196,** 748–759.

Komori, S., Kagiyama, T., Takakura, S., Ohsawa, S., Mimura, M. & Mogi, T., 2013. Effect of the hydrothermal alteration on the surface conductivity of rock matrix: comparative study between relatively-high and low temperature hydrothermal systems, *J. Volc. Geotherm. Res.,* **264,** 164–171.

Manga, M. *et al.*, 2012. Heat flow in the Lesser Antilles island arc andadjacent back arc Grenada basin, *Geochem. Geophys. Geosyst.,* **13,** 1–19.

Mathieu, L., 2010. The structure of Guadeloupe, Maderas and Mt Cameroon Volcanoes and the impact of strike-slip movements, *PhD thesis,* Université Blaise Pascal - Clermont Ferrand II; Trinity College Dublin.

Matsunaga, Y. & Kanga, W., 2022. Numerical modeling of a volcanic hydrothermal system based on resistivity structure, *J. Disaster Res.,* **17**(5), 654–662.

Minami, T., Utsugi, M., Utada, H., Kagiyama, T. & Inoue, H., 2018. Temporal variation in the resistivity structure of the first Nakadake crater, Aso volcano, Japan, during the magmatic eruptions from November 2014 to May 2015, as inferred by the ACTIVE electromagnetic monitoring system, *Earth, Planets Space,* **70,** doi:10.1186/s40623-018-0909-2.

Navelot, V. *et al.* 2018. Petrophysical properties of volcanic rocks and impacts of hydrothermal alteration in the Guadeloupe Archipelago (West Indies), *Journal of Volcanology and Geothermal Research,* **360,** 1–21. doi:10.1016/j.jvolgeores.2018.07.004.

Navelot, V., 2018. Caractérisations Structurale Et Pétrophysique D'un Système Géothermique En Contexte Volcanique D'arc De Subduction Exemple De L'archipel De Guadeloupe, *PhD thesis,* Université de Lorraine.

Pabst, W., Gregorova, E., Rambaldi, E. & Bignozzi, M.C., 2015. Effective elastic constants of plagioclase feldspar aggregates in dependence of the anorthite content – a concise review, *Ceramics – Silikáty,* **59**(4), 326–330.

Petrillo, Z., D'Auria, L., Mangiacapra, A., Chiodini, G., Caliro, S. & Scippacercola, S., 2019. A perturbative approach for modeling short-term fluid-driven ground deformation episodes on volcanoes: a case study in the Campi Flegrei caldera (Italy), *J. geophys. Res.,* **124,** 1036–1056.

Popov, Y., Beardsmore, G., Clauser, C. & Roy, S., 2016. ISRM suggested methods for determining thermal properties of rocks from laboratory tests at atmospheric pressure, *Rock Mech. Rock Eng.,* **49,** 4179–4207.

Popov, Y.A., Pribnow, D.F.C., Sass, J.H., Williams, C.F. & Burkhardt, H., 1999. Characterization of rock thermal conductivity by high-resolution optical scanning, *Geothermics,* **28,** 253–276.

Revil, A. *et al.*, 2017c. Complex conductivity of soils, *Water Resour. Res.,* **53**(8), 7121–7147.

Revil, A. *et al.*, 2022. Induced polarization images alteration in stratovolcanoes, *J. Volc. Geotherm. Res.,* **429,** doi:10.1016/j.jvolgeores.2022.107598.

Revil, A., 2000. Thermal conductivity of unconsolidated sediments with geophysical applications, *J. geophys. Res.,* **105**(16), 749–716, 768.

Revil, A., 2013. On charge accumulations in heterogeneous porous materials under the influence of an electrical field, *Geophysics,* **78**(4), D271–D291.

Revil, A., Hermitte, D., Spangenberg, E. & Cochémé, J.J., 2002. Electrical properties of zeolitized volcaniclastic materials, *Journal of Geophysical Research,* **107**(B8), 2168. doi:10.1029/2001JB000599.

Revil, A., Le Breton, M., Niu, Q., Wallin, E., Haskins, E. & Thomas, D.M., 2017a. Induced polarization of volcanic rocks –1. Surface versus quadrature conductivity, *Geophys. J. Int.,* **208,** 826–844.

Revil, A., Le Breton, M., Niu, Q., Wallin, E., Haskins, E. & Thomas, D.M., 2017b. Induced polarization of volcanic rocks. 2. Influence of pore size and permeability, *Geophys. J. Int.,* **208,** 814–825.

Revil, A., Qi, Y., Ghorbani, A., Coperey, A., Soueid Ahmed, A., Finizola, A. & Ricci, T., 2019. Induced polarization of volcanic rocks. 3. Imaging clay cap properties in geothermal fields, *Geophys. J. Int.,* **218**(2), 1398–1427.

Revil, A., Qi, Y., Ghorbani, A., Gresse, M. & Thomas, D.M., 2021. Induced polarization of volcanic rocks. 5. Imaging the temperature field of shield volcanoes, *Geophys. J. Int.,* **225,** 1492–1509.

Revil, A., Saracco, G. & Labazuy, P., 2003. The volcano-electric effect, *J. geophys. Res.,* **108**(B5), doi:10.1029/2002JB001835.

Rinaldi, A.P., Todesco, M., Vandemeulebrouck, J., Revil, A. & Bonafede, M., 2011. Electrical conductivity, ground displacement, gravity changes, and gas flow at Solfatara crater (Campi Flegrei caldera, Italy): results from numerical modeling, *J. Volc. Geotherm. Res.,* **207,** 93–105.

Rosener, M., 2007. Etude Pétrophysique Et Modélisation Des Effets Des Transferts Thermiques Entre Roche Et Fluide Dans Le Contexte Géothermique De Soultz-sous-Forêts, *PhD thesis,* Université de Strasbourg.

Soueid Ahmed, A. *et al.*, 2018. 3D electrical conductivity tomography of volcanoes, *J. Volc. Geotherm. Res.,* **356,** 243–263.

Stissi, S.C., Napoli, R., Currenti, G., Afanasyev, A. & Montegrossi, G., 2021. Influence of permeability on the hydrothermal system at Vulcano Island (Italy): inferences from numerical simulations Santina Chiara, *Earth, Planets Space,* **73,** doi:10.1186/s40623-021-01515-z.

Syahbana, D.K., Caudron, C., Jousset, P., Lecocq, T., Camelbeeck, T. & Bernard, A., 2014. Fluid dynamics inside a "wet" volcano inferred from the complex frequencies of long-period (LP) events: an example from Papandayan volcano, West Java, Indonesia, during the 2011 seismic unrest, *J. Volc. Geotherm. Res.,* **280,** 76–89.

Todesco, M. & Berrino, G., 2005. Modeling hydrothermal fluid circulation and gravity signals at the Phlegraean Fields caldera, *Earth planet. Sci. Lett.,* **240**(2), 328–338.

Vaudelet, P., Revil, A., Schmutz, M., Franceschi, M. & Bégassat, P., 2011. Induced polarization signature of the presence of copper in saturated sands, *Water Resour. Res.,* **47,** doi:10.1029/2010WR009310.

Verati, C., Mazabraud, Y., Lardeaux, J.-M., Corsini, M., Schneider, D., Voitus, E. & Zami, F., 2016. Tectonic evolution of Les Saintes Archipelago (Guadeloupe, French West Indies); relation with the Lesser Antilles arc system, *Bull. Soc. Geol. Fr.,* **187,** 3–10.

Watanabe, N., Mogi, T., Yamaya, Y., Kitamura, K., Asanuma, H. & Tsushiya, N., 2022. Electrical conductivity of H_2O-NaCl fluids under supercritical geothermal conditions and implications for deep conductors observed by the magnetotelluric method, *Geothermics,* **101,** doi:10.1088/1361-6501/ab1b09.

Waxman, M.H. & Smits, L.J.M., 1968. Electrical conductivities in oil bearing shaly sands, *Soc. Pet. Eng. J.,* **8,** 107–122.

Wyering, L.D., Villeneuve, M.C., Wallis, I.C., Siratovicha, P.A., Kennedy, B.M., Gravleya, D.M. & Cant, J.L., 2014. Mechanical and physical properties of hydrothermally altered rocks, Taupo Volcanic Zone, New Zealand, *J. Volc. Geotherm. Res.,* **288,** 76–93.

Zhan, Y., Le Mével, H., Roman, D.C., Giroa, T. & Gregg, P.M., 2022. Modeling deformation, seismicity, and thermal anomalies driven by degassing during the 2005-2006 pre-eruptive unrest of Augustine Volcano, Alaska, *Earth planet. Sci. Lett.,* **585,** doi:10.1016/j.epsl.2022.117524.

Zimmermann, E., Huisman, J.A., Mester, A. & van Waasen, S., 2019. Correction of phase errors due to leakage currents in wideband EIT field measurements on soil and sediments, *Meas. Sci. Technol.,* **30**(8), doi:10.1088/1361-6501/ab1b09.

Zimmermann, E., Kemna, A., Berwix, J., Glaas, W., Münch, H.M. & Huisman, J.A., 2008. A high-accuracy impedance spectrometer for measuring sediments with low polarizability, *Meas. Sci. Technol.,* **19**(10), doi:10.1088/0957-0233/19/10/105603.